Scientific Research Publishing

Advances in Nanoparticles, 2025, 14(4), 173-208
https://www.scirp.org/journal/anp
ISSN Online: 2169-0529
ISSN Print: 2169-0510

Machine Learning-Driven Prediction and Analysis of Magnetohydrodynamic (MHD) Natural Convection in Nanofluid-Filled Trapezoidal Cavities with Variable Obstacle Shapes, Wall Corrugations, and Inclination Angles

Sree Pradip Kumer Sarker*, Md. Mahmud Alam

Department of Mathematics, Dhaka University of Engineering and Technology (DUET), Gazipur-1707, Bangladesh
Email: *pradip.duet@gmail.com, alamdr.mahmud@duet.ac.bd

How to cite this paper: Sarker, S.P.K. and Alam, M.M. (2025) Machine Learning-Driven Prediction and Analysis of Magnetohydrodynamic (MHD) Natural Convection in Nanofluid-Filled Trapezoidal Cavities with Variable Obstacle Shapes, Wall Corrugations, and Inclination Angles. *Advances in Nanoparticles*, **14**, 173-208.
https://doi.org/10.4236/anp.2025.144011

Received: October 19, 2025
Accepted: November 10, 2025
Published: November 10, 2025

Abstract

This study proposes a machine learning-enhanced framework to predict and analyze magnetohydrodynamic (MHD) natural convection within nanofluid-filled trapezoidal cavities featuring variable obstacle shapes, wall corrugations, and inclination angles. A comprehensive dataset was generated through Finite Element Method (FEM) simulations covering a wide parametric range, including Rayleigh numbers (10^3 - 10^6) and Hartmann numbers (0 - 50), for Cu-H_2O nanofluids. Key thermal performance metrics Nusselt number (Nu), entropy generation (S_T), and Ecological Coefficient of Performance (ECOP), were extracted and used to train supervised machine learning models: Support Vector Regression (SVR), Decision Tree (DT), and Random Forest (RF). Among them, the RF model achieved superior performance, yielding R^2 scores of 0.991 (Nu), 0.982 (St), and 0.989 (ECOP), with mean prediction errors under 1.5%. The results show excellent agreement between FEM and ML outputs across diverse configurations, including different obstacle geometries (star, square, triangular), wall undulations (sinusoidal, square, triangular), and inclination angles (15˚, 30˚, 45˚). The integration of ML significantly reduced computational cost while preserving high accuracy, thus demonstrating its viability for rapid prediction and optimization. This hybrid FEM-ML methodology offers a powerful tool for real-time thermal system analysis and design in advanced MHD nanofluid applications.

Keywords

Magnetohydrodynamic (MHD) Convection, Nanofluid, Machine Learning Prediction, Trapezoidal Cavity, Thermal Performance Analysis

1. Introduction

Natural convection in enclosures has long been a cornerstone topic in thermal engineering, owing to its critical role in a wide range of applications, including solar thermal collectors, electronic cooling systems, and energy-efficient architectural designs [1]. These systems depend heavily on passive heat transfer mechanisms to regulate temperature and ensure operational efficiency. Over the past few decades, the performance of such systems has been significantly improved through the introduction of nanofluids engineered by dispersing nanoparticles in traditional base liquids. These nanoparticle suspensions enhance the thermophysical properties of the fluid, particularly thermal conductivity and heat capacity, thereby improving the rate and uniformity of convective heat transfer within enclosures [2] [3].

The behavior of nanofluid-based convection is not only influenced by the base fluid and nanoparticle type but also by a range of physical and geometric parameters. Studies have demonstrated that internal features such as heated bodies or obstructions, the inclination of the cavity, external magnetic fields, and specific boundary conditions all play crucial roles in shaping the flow and thermal fields [4]-[6]. For example, incorporating internal elliptical or circular obstacles within a square cavity with a wavy top wall has been shown to disrupt conventional flow patterns, resulting in enhanced mixing and heat transfer [7]. These findings highlight the importance of internal geometry and boundary configuration in optimizing convective behavior.

As engineering systems continue to increase in complexity, particularly in microscale and compact heat exchanger designs, the use of nanofluids in non-standard and irregular enclosures has attracted growing research attention. Among the computational tools employed, the Finite Element Method (FEM) stands out for its capacity to handle complex boundaries and heterogeneous materials with high numerical precision [8]. FEM-based simulations allow detailed resolution of the velocity, temperature, and pressure fields in domains where analytical or simplified numerical methods fall short. However, the primary limitation of FEM is its high computational cost, especially when applied to broad parametric studies or real-time optimization tasks.

To address this limitation, Machine Learning (ML) has emerged as a powerful and complementary approach. By training on datasets generated through high-fidelity simulations such as FEM, ML models can serve as surrogate predictors that provide fast and accurate estimations of thermal behavior without the need for solving complex differential equations repeatedly [9]-[11]. In particular, ML has

proven effective in predicting nanofluid thermal properties and convective performance across various geometrical and operational settings [12]. Motivated by these developments, the current study proposes a hybrid framework that integrates FEM and ML to analyze the heat transfer characteristics and entropy generation in trapezoidal cavities filled with Cu-H_2O nanofluid and containing internally heated star-shaped, square, and triangular obstacles. The framework also incorporates magnetohydrodynamic (MHD) effects by applying external magnetic fields across the cavity.

The geometry of internal obstacles has a pronounced impact on fluid motion and heat transfer. Shapes such as circular, elliptical, square, and triangular affect vortex formation, thermal gradients, and Nusselt number distribution, all of which contribute to the overall thermal resistance of the system [13]-[17]. Furthermore, the number, placement, and orientation of these obstacles also influence entropy generation and convective flow structure [18] [19]. Another critical factor is the inclination of the cavity itself. Varying the inclination angle modifies the effective direction of buoyancy forces, thereby altering flow intensity, thermal stratification, and energy dissipation due to thermodynamic irreversibility [20]-[24]. Some studies have even identified specific inclination angles that optimize thermal efficiency by enhancing heat transfer while suppressing entropy production [25].

External magnetic fields introduce yet another layer of control, quantified by the Hartmann number. The Lorentz force generated by these fields tends to suppress fluid motion, shifting the heat transfer mechanism from convection-dominated to conduction-dominated regimes [26]-[31]. However, when optimized, MHD effects can lead to improved temperature uniformity and thermal regulation, especially in electrically conducting nanofluids like Cu-H_2O [32].

Beyond internal obstacles and magnetic fields, wall modifications such as introducing wavy or corrugated top boundaries have also been shown to disrupt the thermal boundary layer, generate secondary vortices, and amplify convective mixing [33]-[36]. These geometric perturbations further contribute to enhanced heat transfer and entropy management, underscoring the multifactorial nature of natural convection in nanofluid-filled cavities.

Recent studies have demonstrated the effectiveness of machine learning (ML) in modeling complex heat transfer phenomena. ML has been used to predict radiative nanofluid behavior [37], replace CFD for forced convection with high accuracy and efficiency [35], and estimate Nusselt numbers in natural convection within helical coils [38]. ML models have also shown strong predictive power in systems involving counter-rotating cylinders [39] and microchannel heat sinks with complex geometries [40]. These efforts support the use of ML in capturing nonlinear thermal behaviors, complementing conventional numerical methods.

The present study aims to bridge this research gap by developing a machine learning-driven predictive framework trained on FEM-generated simulation data to model the coupled effects of magnetic field intensity, wall corrugation, obstacle

geometry, and inclination angle on heat transfer, entropy generation, and overall thermal performance in Cu-H_2O nanofluid-filled trapezoidal cavities. By combining the precision of FEM with the computational efficiency of ML, this work provides a hybrid platform for accurate, fast, and scalable analysis of MHD natural convection, thereby contributing to the advancement of intelligent thermal management and optimization systems.

2. Materials and Methods

This study explores natural convection and entropy generation in a two-dimensional trapezoidal enclosure filled with a Cu-H_2O nanofluid ($\varphi = 0.02$). The trapezoidal cavity features a fixed base angle of $\gamma = 15^\circ$ and is inclined at angles $\lambda = 15^\circ$, 30°, and 45° to investigate the influence of gravitational orientation on thermal and flow characteristics. Two internal heat-generating solid obstacles, designed as star, square, or triangle shapes, are symmetrically embedded at the center of the cavity. The top boundary is geometrically modified using sinusoidal, square, or triangular corrugations to assess the impact of surface undulations on convective flow. Figures 1-3 illustrate these configurations.

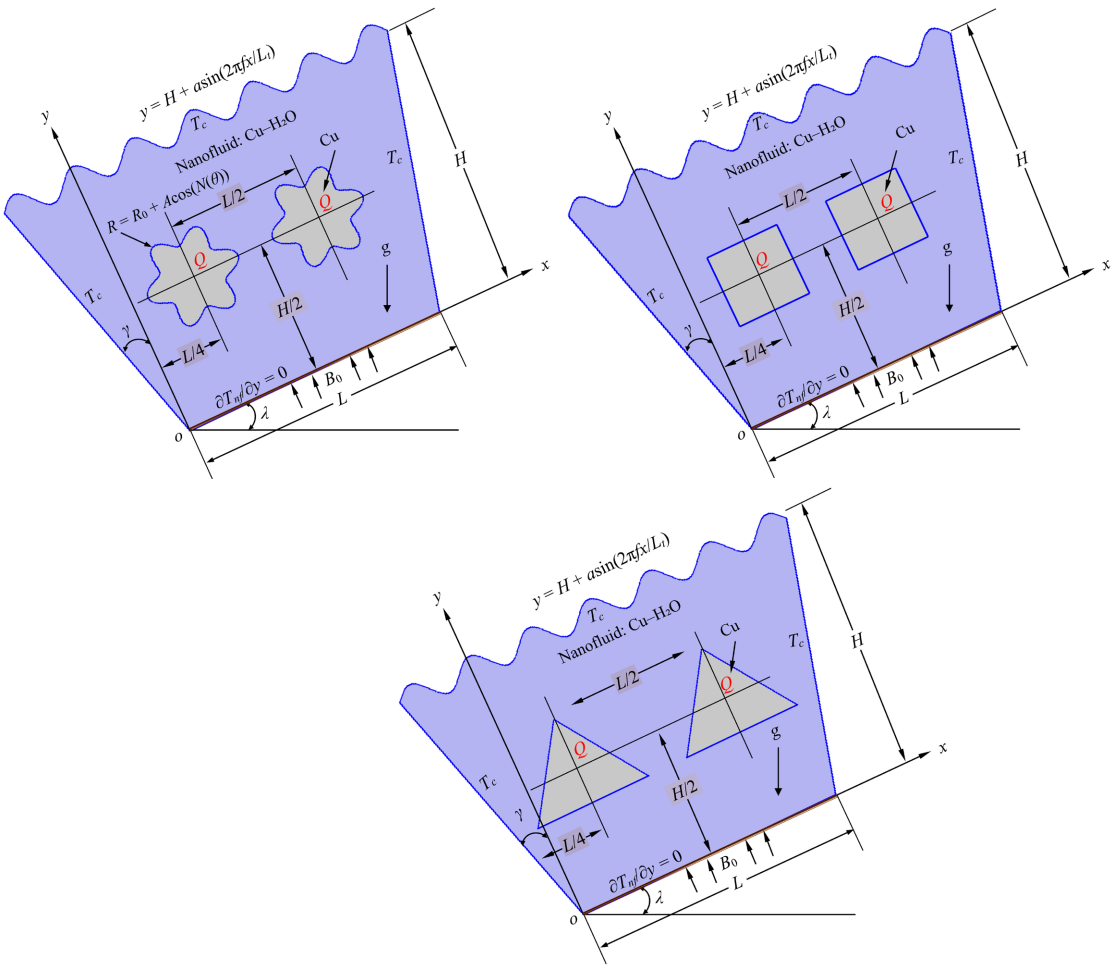

Figure 1. Different geometry with sinusoidal corrugation.

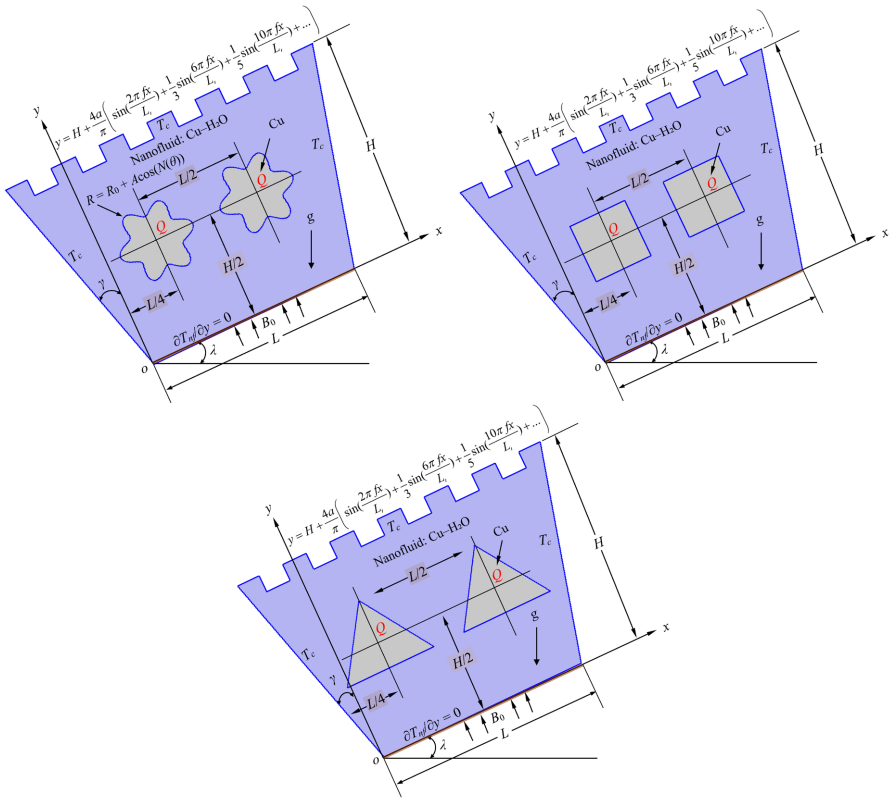

Figure 2. Different geometry with square corrugation.

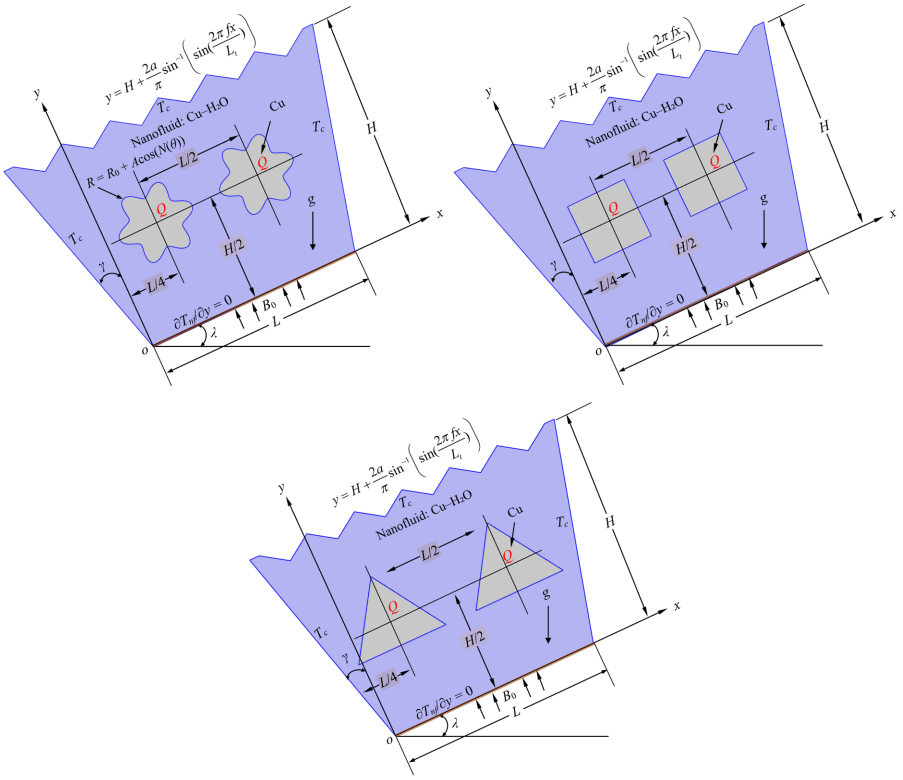

Figure 3. Different geometry with triangular corrugation.

A uniform horizontal magnetic field is applied across the cavity to induce magnetohydrodynamic (MHD) effects. The top and vertical side walls are maintained at a constant cold temperature, while the inclined bottom wall is adiabatic. All walls, including embedded solid surfaces, obey no-slip boundary conditions. The embedded obstacles serve as internal volumetric heat sources, uniformly generating thermal energy.

The governing equations are based on the conservation of mass, momentum, energy, and entropy generation, accounting for nanofluid properties, buoyancy-driven flow, and MHD interactions are described in below ([5] [17] [31] [32]):

For Sinusoidal wavy top wall:

$$y = H + a\sin\left(\frac{2\pi fx}{L_t}\right) \tag{1}$$

For Square wavy top wall:

$$y = H + \frac{4a}{\pi}\left(\sin\left(\frac{2\pi fx}{L_t}\right) + \frac{1}{3}\sin\left(\frac{6\pi fx}{L_t}\right) + \frac{1}{5}\sin\left(\frac{10\pi fx}{L_t}\right) + \cdots\right) \tag{2}$$

For Triangular wavy top wall:

$$y = H + \frac{2a}{\pi}\sin^{-1}\left(\sin\left(\frac{2\pi fx}{L_t}\right)\right) \tag{3}$$

here, H : Height of the cavity, a : Amplitude of the wave, f : Frequency (number of waves), L_t : Total length of the top wall, and x is the position along the wall.

Gravitational acceleration g acts vertically downward, but is decomposed into components along the inclined axis:

$$g_x = g\sin(\lambda), g_y = -g\cos(\lambda) \tag{4}$$

Fluid domain:

$$\frac{\partial u}{\partial x} + \frac{\partial v}{\partial y} = 0 \tag{5}$$

$$\begin{aligned}&\rho_{nf}\left(u\frac{\partial u}{\partial x} + v\frac{\partial u}{\partial y}\right)\\ &= -\frac{\partial p}{\partial x} + \mu_{nf}\left(\frac{\partial^2 u}{\partial x^2} + \frac{\partial^2 u}{\partial y^2}\right) + \rho_{nf} g\beta_{nf}\left(T_{nf} - T_c\right)\sin(\lambda) - \sigma_{nf}B_0^2 u\end{aligned} \tag{6}$$

$$\rho_{nf}\left(u\frac{\partial v}{\partial x} + v\frac{\partial v}{\partial y}\right) = -\frac{\partial p}{\partial y} + \mu_{nf}\left(\frac{\partial^2 v}{\partial x^2} + \frac{\partial^2 v}{\partial y^2}\right) + \rho_{nf} g\beta_{nf}\left(T_{nf} - T_c\right)\cos(\lambda) \tag{7}$$

$$\rho_{nf}C_{p,nf}\left(u\frac{\partial T_{nf}}{\partial x} + v\frac{\partial T_{nf}}{\partial y}\right) = k_{nf}\left(\frac{\partial^2 T_{nf}}{\partial x^2} + \frac{\partial^2 T_{nf}}{\partial y^2}\right) \tag{8}$$

Star-shaped solid domains:

$$k_s\left(\frac{\partial^2 T_s}{\partial x^2} + \frac{\partial^2 T_s}{\partial y^2}\right) + Q = 0 \tag{9}$$

here, u and v denote velocity components in the x- and y-directions, respectively, and p and T represent pressure and temperature, respectively. The fluid properties are mass density (ρ), thermal conductivity (k), specific heat at constant pressure (C_p), volumetric thermal expansion coefficient (β), and electrical conductivity (σ).

Dimensional Boundary Conditions:

Top Wall:

$$u = v = 0, \quad T = T_c \tag{10}$$

Inclined Side Wall:

$$u = v = 0, \quad T = T_c \tag{11}$$

Bottom Wall:

$$u = v = 0, \quad \frac{\partial T}{\partial x} = 0 \tag{12}$$

Heated Block:

An internal heat-generation rate of $Q = 1 \times 10^6$ W/m^3 was used for obstacles, consistent with prior studies [37] on thermally active enclosures. Sensitivity analysis showed <3% variation in Nusselt number across typical Q ranges, confirming this value's suitability. The continuity of temperature and heat flux at fluid-solid interfaces is enforced:

$$T_{Fluid} = T_{Solid}, \quad k_{nf} \frac{\partial T}{\partial n_{Fluid}} = k_s \frac{\partial T}{\partial n_{Solid}} \tag{13}$$

$$\rho_{nf} = (1-\phi)\rho_f + \phi\rho_s \tag{14}$$

$$(\rho c_p)_{nf} = (1-\phi)(\rho c_p)_f + \phi(\rho c_p)_s \tag{15}$$

$$\mu_{nf} = \frac{\mu_f}{(1-\phi)^{2.5}} \tag{16}$$

$$k_{nf} = k_f \left[\frac{k_s + 2k_f - 2\phi(k_f - k_s)}{k_s + 2k_f + \phi(k_f - k_s)} \right] \tag{17}$$

$$\beta_{nf} = \frac{(1-\phi)\rho_f\beta_f + \phi\rho_s\beta_s}{\rho_{nf}} \tag{18}$$

Entropy production reflects energy loss from irreversible effects like heat transfer, friction, and MHD forces. In buoyancy-driven MHD flow, entropy is generated through heat transfer, viscous dissipation, and magnetic fields. The local entropy generation due to heat transfer (S_{ht}) in solid and fluid domains is given by:

$$S_{ht} = \frac{k_s}{T_s^2}\left[\left(\frac{\partial T_s}{\partial x}\right)^2 + \left(\frac{\partial T_s}{\partial y}\right)^2\right] + \frac{k_{nf}}{T_{nf}^2}\left[\left(\frac{\partial T_{nf}}{\partial x}\right)^2 + \left(\frac{\partial T_{nf}}{\partial y}\right)^2\right] + \frac{Q_{gen}}{T_s} \tag{19}$$

The local volumetric entropy production due to viscous flow dissipation (S_{ff}) and external magnetic effects (S_{mf}) can be described using the following formulas [5] [17] [31] [32]:

$$S_{ff} = \frac{\mu_{nf}}{T_{nf}}\left[2\left(\frac{\partial u}{\partial x}\right)^2 + 2\left(\frac{\partial v}{\partial y}\right)^2 + \left(\frac{\partial u}{\partial y} + \frac{\partial v}{\partial x}\right)^2\right] \tag{20}$$

$$S_{mf} = \beta_0^2 \frac{\sigma_{nf}}{T_{nf}} v^2 \tag{21}$$

To get the non-dimensional governing equations, the following scales are used:

$$X = \frac{x}{L}, Y = \frac{y}{L}, U = \frac{uL}{\alpha_f}, V = \frac{vL}{\alpha_f}, \theta = \frac{T - T_c}{T_h - T_c}, P = \frac{pL^2}{\mu_{nf}}, \text{Here}, \alpha_f = \frac{k_f}{\rho_f c_{p,f}} \tag{22}$$

$$Ra = \frac{g\beta_{nf}\left(T_h - T_c\right)L^3}{\nu_{nf}\alpha_f}, Pr = \frac{\nu_f}{\alpha_f}, Ha = \beta_0 L\sqrt{\frac{\sigma_{nf}}{\mu_{nf}}}, Q^* = \frac{QL^2}{k_{nf}\left(T_h - T_c\right)} \tag{23}$$

$$\frac{\partial U}{\partial X} + \frac{\partial V}{\partial Y} = 0 \tag{24}$$

$$U\frac{\partial U}{\partial X} + V\frac{\partial U}{\partial Y} = -\frac{\partial P}{\partial X} + \frac{\mu_{nf}}{\mu_f}\left(\frac{\partial^2 U}{\partial X^2} + \frac{\partial^2 U}{\partial Y^2}\right) + RaPr\frac{\rho_{nf}\beta_{nf}}{\rho_f\beta_f}\theta\sin(\lambda) - Ha^2 U \tag{25}$$

$$U\frac{\partial V}{\partial X} + V\frac{\partial V}{\partial Y} = -\frac{\partial P}{\partial X} + \frac{\mu_{nf}}{\mu_f}\left(\frac{\partial^2 V}{\partial X^2} + \frac{\partial^2 V}{\partial Y^2}\right) + RaPr\frac{\rho_{nf}\beta_{nf}}{\rho_f\beta_f}\theta\cos(\lambda) \tag{26}$$

$$U\frac{\partial \theta}{\partial X} + V\frac{\partial \theta}{\partial Y} = \frac{k_{nf}}{k_f}\frac{1}{Pr}\left(\frac{\partial^2 \theta}{\partial X^2} + \frac{\partial^2 \theta}{\partial Y^2}\right) \tag{27}$$

$$\frac{k_s}{k_{nf}}\left(\frac{\partial^2 \theta_s}{\partial X^2} + \frac{\partial^2 \theta_s}{\partial Y^2}\right) + Q^* = 0 \tag{28}$$

Non-Dimensional Boundary Conditions:

Top Wall:

$$U = V = 0, \quad T = T_c \tag{29}$$

Inclined Side Wall:

$$U = V = 0, \quad T = T_c \tag{30}$$

Bottom Wall:

$$U = V = 0, \quad \frac{\partial T}{\partial X} = 0 \tag{31}$$

Heated Block:

Internal volumetric heat generation applied in the solid domain, $Q > 0$; continuity of temperature and heat flux at fluid-solid interfaces are enforced:

$$T_{Fluid} = T_{Solid}, \quad k_{nf}\frac{\partial T}{\partial N_{Fluid}} = k_s\frac{\partial T}{\partial N_{Solid}} \tag{32}$$

Non-Dimensional Nanofluid Properties:

$$\frac{\rho_{nf}}{\rho_f} = (1 - \phi) + \phi\frac{\rho_s}{\rho_f} \tag{33}$$

$$\frac{(\rho c_p)_{nf}}{(\rho c_p)_f} = (1-\phi) + \phi \frac{(\rho c_p)_s}{(\rho c_p)_f} \tag{34}$$

$$\frac{\mu_{nf}}{\mu_f} = \frac{1}{(1-\phi)^{2.5}} \tag{35}$$

$$\frac{k_{nf}}{k_f} = \frac{k_s + 2k_f - 2\phi(k_f - k_s)}{k_s + 2k_f + \phi(k_f - k_s)} \tag{36}$$

$$\beta_{nf}\rho_{nf} = (1-\phi)\rho_f\beta_f + \phi\rho_s\beta_s \tag{37}$$

The thermal behavior of the chamber under different operating conditions is assessed by analyzing the Nusselt number (Nu) of the heated strips and the average fluid temperature (Θ_{av}) inside the domain. The definitions of these quantities are as follows:

$$\mathrm{Nu} = \frac{L}{L_s}\left[-\int_{L_0/L}^{2L_0/L}\left.\frac{\partial\Theta}{\partial Y}\right|_{Y=0}\mathrm{d}X - \int_{3L_0/L}^{4L_0/L}\left.\frac{\partial\Theta}{\partial Y}\right|_{Y=0}\mathrm{d}X\right], \Theta_{av} = \frac{1}{A}\int_A \Theta \mathrm{d}A, \tag{38}$$

here, A represents the non-dimensional surface area of the fluid domain, X and Y are the dimensionless Cartesian coordinates, U and V indicate dimensionless velocity components, and P and Θ are the non-dimensional pressure and temperature of the nanofluid, respectively.

The total entropy generation, expressed as a dimensionless quantity, can be obtained using the following expression:

$$S_T = \frac{T_c^2 L^2}{k_f \Delta T^2 A}\int_A \left(S_{ht} + S_{ff} + S_{mf}\right)\mathrm{d}A \tag{39}$$

where A represents the surface area of the computational domain.

The Ecological Coefficient of Performance (ECOP) can be defined as follows to provide a relative estimate of total entropy production associated with heat transfer:

$$\mathrm{ECOP} = \frac{S_T}{Nu} \tag{40}$$

The working fluid is a Cu-H_2O nanofluid with a fixed nanoparticle volume fraction of $\varphi = 0.02$, selected for its superior thermal conductivity and MHD compatibility. Simulations are conducted across a Rayleigh number range of 10^3 to 10^6 and Hartmann number (Ha) range from 0 to 50. The working fluid's properties at a reference temperature of 300 K are presented in Table 1(a). These properties are essential for modeling buoyancy-driven convection, MHD behavior, and entropy generation.

The Galerkin Finite Element Method (FEM) is employed to numerically solve the coupled governing equations under the defined boundary and initial conditions. To complement the Finite Element Method (FEM) simulations and accelerate the prediction of thermal performance metrics, a supervised Machine Learning (ML) framework was developed. The aim was to model the relationship be-

tween physical/geometric parameters and target thermal responses, namely, Nusselt number (Nu), Entropy Generation (S_T), and Ecological Coefficient of Performance (ECOP).

To ensure the numerical accuracy of the FEM simulations, a detailed mesh analysis was conducted for different obstacle shapes: square, star, and triangular blocks. As shown in Table 1(b), each mesh configuration includes a mix of triangular and quadrilateral elements, with total element counts ranging from 17,986 to 21,964. The average element quality remains above 0.77 for all cases, with the square block mesh achieving the highest quality at 0.8026.

Table 1. (a): Thermo-physical properties of Water and Cu at T_m = 300K ([5] [17] [31] [32]); (b): Mesh Statistics for Wavy-Top Trapezoidal Cavity with different Heated Blocks.

(a)

Name of Property	Symbol	Unit	Water	Cu
Mass Density	ρ	$kg{\cdot}m^{-3}$	996.6	8933
Specific Heat at Constant Pressure	C_p	$J{\cdot}kg^{-1}{\cdot}K^{-1}$	4179.2	385
Thermal Conductivity	k	$W{\cdot}m^{-1}{\cdot}K^{-1}$	0.6102	401
Volumetric Thermal Expansion Coefficient	β	K^{-1}	26.6×10^{-5}	49.9×10^{-6}
Electrical Conductivity	σ	$S{\cdot}m^{-1}$	0.05	59.6×10^{-6}
Dynamic viscosity	μ	$kg{\cdot}m^{-1}{\cdot}s^{-1}$	8.538×10^{-4}	-
Prandtl Number	Pr	-	5.856	-

(b)

Parameter	Value Square Blocks	Value Star Blocks	Value Triangular Blocks
Mesh vertices	10,756	11,990	9900
Element type	All elements	All elements	All elements
Triangular elements	18,300	20,368	16,598
Quadrilateral elements	1396	1596	1388
Edge elements	714	798	706
Vertex elements	12	8	10
Total number of elements	19,696	**21,964**	17,986
Minimum element quality	0.2356	0.1379	0.2297
Average element quality	0.8026	0.7778	0.8004
Element area ratio	0.003044	0.004769	0.003075
Total mesh area	3.178×10^{-7} m^2	3.178×10^{-7} m^2	3.178×10^{-7} m^2

The minimum element quality and element area ratios confirm that the meshes are sufficiently refined for accurate thermal field resolution. Additionally, the total mesh area remains consistent across cases (3.178×10^{-7} m^2), indicating geometric fidelity. Time-step convergence was validated separately using steps of 0.01, 0.005,

and 0.002 s, showing negligible variation in Nusselt number predictions (<1.5%), confirming temporal resolution adequacy.

The dataset for training and testing was generated from 324 FEM simulations, covering diverse combinations of input parameters, including Rayleigh number (Ra), Hartmann number (Ha), nanoparticle volume fraction (φ), obstacle shape, wall corrugation type, and cavity inclination angle (λ). These features spanned broad ranges—$Ra = 10^3$ - 10^6, Ha = 0 - 50, and $\lambda = 15^\circ$ - 45° ensuring comprehensive ML coverage. FEM-derived Nusselt number (Nu), entropy generation (S_T), and energy conversion performance (ECOP) were used as target variables. Prior to training, continuous features were normalized, and categorical features were one-hot encoded. The dataset was randomly split into 80% training (259 cases) and 20% testing (65 cases) to evaluate generalization. Three regression models were employed in this study: Random Forest, Support Vector Regression, and Extreme Gradient Boosting.

1) Support Vector Regression (SVR) using a radial basis function (RBF) kernel;

2) Decision Tree Regression (DT) for rule-based partitioning of the feature space;

3) Random Forest Regression (RF) as an ensemble learning method for robust nonlinear prediction.

Model development was performed using Python's *scikit-learn* library. Hyperparameters were optimized via grid search and five-fold cross-validation to prevent overfitting and ensure stability. The trained models were subsequently used to establish a predictive framework that offers a fast and accurate alternative to traditional FEM-based simulations for evaluating the impact of MHD, nanofluid dynamics, and cavity geometry on thermal performance.

3. Validation

To ensure the accuracy and reliability of the present numerical model, a validation study was conducted by comparing the simulation results with the benchmark work of Abdelmalek *et al.* [17]. The comparison focused on thermal profiles and average Nusselt number values under equivalent conditions. As illustrated in **Figure 4**, both studies exhibit closely matching isotherm distributions around star-shaped internal obstacles at a Rayleigh number of $Ra = 10^4$. The present simulation demonstrates smoother and more symmetric thermal contours, which can be attributed to the use of a finer computational mesh and higher spatial resolution. This strong agreement confirms the validity of the adopted numerical approach in accurately capturing the key thermofluidic behaviors in MHD-assisted nanofluid convection within trapezoidal enclosures.

Table 2 reinforces the validation results, showing that the deviation in average Nusselt numbers remains below 1.5% across the Rayleigh number range of 10^3 to 10^6. This confirms both the accuracy and numerical stability of the present FEM-based model. The findings also emphasize the critical influence of geometric complexity and cavity inclination on heat transfer performance in magnetically actu-

ated nanofluid systems. Notably, configurations combining wall corrugation with non-circular obstacles, such as star or triangular shapes, exhibit improved passive thermal regulation, demonstrating their effectiveness in enhancing natural convection under MHD conditions.

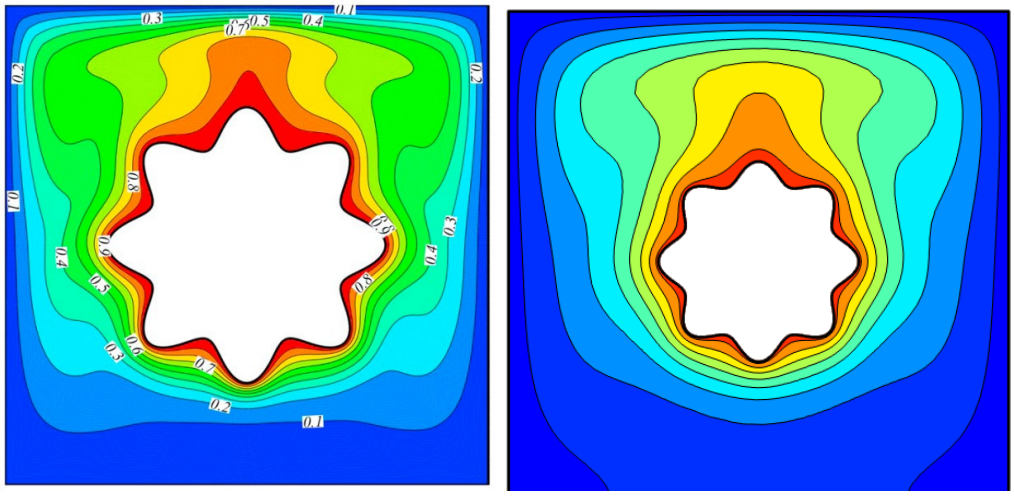

Abdelmalek *et al.* [17] Present Work

Figure 4. Isotherms for different values of $Ra = 10^4$ when $N = 8$, $A = 0.15$, $\phi = 2\%$.

Table 2. Comparison of *Nu* between present work and Abdelmalek *et al.* [17].

Ra	Nanoparticle Volume Fraction (ϕ %)	Present Study	Abdelmalek *et al.* [17]	Deviation (%)
10^3	2	1.1470	1.1307	1.44
10^4	2	2.2944	2.2674	1.19
10^5	2	4.6379	4.5851	1.15
10^6	2	8.9586	8.8341	1.41

4. Results and Discussion

This section presents the outcomes of the numerical and data-driven investigations into MHD natural convection in nanofluid-filled trapezoidal cavities. The results are divided into two parts: the first outlines the detailed Finite Element Method (FEM) simulations conducted across various geometric and physical configurations; the second discusses the implementation and evaluation of machine learning models trained on FEM data to predict key thermal performance indicators. Both approaches aim to assess the effects of obstacle shape, wall corrugation, inclination angle, and magnetic field strength on heat transfer (*Nu*), entropy generation (S_T), and ecological performance (ECOP).

4.1. FEM Simulation Results Analysis

The finite element simulations generated extensive data capturing the influence of geometric and physical parameters on heat transfer and entropy-related behav-

ior in MHD-driven nanofluid convection. The results are structured into three key performance indicators: Nusselt number (Nu), Entropy generation (S_T), and Ecological Coefficient of Performance (ECOP), each analyzed based on variations in obstacle geometry, wall corrugation, inclination angle, Rayleigh number, and Hartmann number. A comprehensive summary of these results is provided in Tables 3-29.

Table 3. Nu for star-shaped obstacles with different Wavy Walls at $\lambda = 15^{\circ}$.

Wavy Wall	Ra	$Ha = 0$	$Ha = 15$	$Ha = 30$	$Ha = 50$
Sinusoidal	10^3	0.79369	0.79369	0.79369	0.79369
	10^4	2.5581	2.5556	2.5533	2.5524
	10^5	3.7556	3.6201	3.4447	3.3369
	10^6	5.7976	5.6067	5.22	4.7166
Square	10^3	0.8018	0.80179	0.80179	0.80179
	10^4	2.6423	2.6404	2.6388	2.6381
	10^5	3.7957	3.6868	3.546	3.4642
	10^6	5.7179	5.5281	5.1568	4.6751
Triangular	10^3	0.79861	0.79861	0.79861	0.79861
	10^4	2.6093	2.6072	2.6054	2.6046
	10^5	3.7736	3.657	3.5047	3.4136
	10^6	5.747	5.5586	5.184	4.6923

Table 4. Nu for Square-Shaped Obstacles with different Wavy Walls at $\lambda = 15^{\circ}$.

Wavy Wall	Ra	$Ha = 0$	$Ha = 15$	$Ha = 30$	$Ha = 50$
Sinusoidal	10^3	0.84326	0.84326	0.84325	0.84324
	10^4	2.6913	2.6881	2.6853	2.684
	10^5	3.9788	3.8277	3.6309	3.5065
	10^6	6.2373	6.0384	5.6553	5.1434
Square	10^3	0.85297	0.85296	0.85295	0.85295
	10^4	2.7849	2.7824	2.7801	2.7792
	10^5	4.0265	3.9039	3.7424	3.6451
	10^6	6.1573	5.9757	5.6151	5.1105
Triangular	10^3	0.84944	0.84943	0.84942	0.84941
	10^4	2.7491	2.7464	2.744	2.7429
	10^5	4.001	3.8709	3.698	3.5913
	10^6	6.1799	5.9944	5.6292	5.1242

Table 5. *Nu* for Triangular-Shaped Obstacles with different Wavy Walls at $\lambda = 15^{\circ}$.

Wavy Wall	*Ra*	*Ha* = 0	*Ha* = 15	*Ha* = 30	*Ha* = 50
Sinusoidal	10^3	0.79176	0.79175	0.79175	0.79174
	10^4	2.9106	2.91	2.9094	2.909
	10^5	4.2103	4.113	4.0332	3.9932
	10^6	6.3746	6.1018	5.6317	5.0893
Square	10^3	0.79783	0.79783	0.79783	0.79783
	10^4	2.9817	2.9813	2.9808	2.9806
	10^5	4.2685	4.2055	4.1485	4.1193
	10^6	6.2743	6.007	5.565	5.0441
Triangular	10^3	0.79608	0.79607	0.79607	0.79607
	10^4	2.9563	2.9558	2.9553	2.955
	10^5	4.2449	4.1709	4.106	4.0729
	10^6	6.3262	6.0564	5.6118	5.073

Table 6. *Nu* for Star-Shaped Obstacles with different Wavy Walls at $\lambda = 30^{\circ}$.

Wavy Wall	*Ra*	*Ha* = 0	*Ha* = 15	*Ha* = 30	*Ha* = 50
Sinusoidal	10^3	0.79369	0.79369	0.79369	0.79369
	10^4	2.5573	2.555	2.5531	2.5523
	10^5	3.7274	3.5914	3.4249	3.3284
	10^6	5.916	5.5713	5.1574	4.6587
Square	10^3	0.80179	0.80179	0.80179	0.80179
	10^4	2.6417	2.64	2.6386	2.6381
	10^5	3.768	3.6621	3.5307	3.4579
	10^6	5.7008	5.4812	5.1053	4.6249
Triangular	10^3	0.79861	0.79861	0.79861	0.79861
	10^4	2.6086	2.6068	2.6052	2.6046
	10^5	3.746	3.6311	3.4879	3.4066
	10^6	5.7559	5.5104	5.1294	4.6408

Table 7. *Nu* for Square-Shaped Obstacles with different Wavy Walls at $\lambda = 30^{\circ}$.

Wavy Wall	*Ra*	*Ha* = 0	*Ha* = 15	*Ha* = 30	*Ha* = 50
Sinusoidal	10^3	0.84326	0.84325	0.84325	0.84324
	10^4	2.6903	2.6874	2.685	2.6839
	10^5	3.9427	3.7923	3.606	3.4952
	10^6	6.3086	5.9994	5.5697	5.0505

Continued

Square	10^3	0.85297	0.85296	0.85295	0.85294
	10^4	2.784	2.7818	2.7799	2.7791
	10^5	3.9912	3.8722	3.7221	3.6364
	10^6	6.1538	5.9156	5.5258	5.0209
Triangular	10^3	0.84943	0.84943	0.84942	0.84941
	10^4	2.7482	2.7458	2.7437	2.7428
	10^5	3.9661	3.8382	3.6762	3.5817
	10^6	6.2045	5.9456	5.5448	5.0349

Table 8. *Nu* for Triangular-Shaped Obstacles with different Wavy Walls at $\lambda = 30^\circ$.

Wavy Wall	*Ra*	*Ha* = 0	*Ha* = 15	*Ha* = 30	*Ha* = 50
Sinusoidal	10^3	0.7917	0.79175	0.79175	0.79174
	10^4	2.9107	2.91	2.9093	2.909
	10^5	4.2444	4.1236	4.0301	3.9908
	10^6	6.4336	6.1422	5.6355	5.062
Square	10^3	0.79783	0.79783	0.79783	0.79783
	10^4	2.9818	2.9812	2.9808	2.9805
	10^5	4.2976	4.2133	4.1464	4.1175
	10^6	6.3298	6.0446	5.5635	5.0332
Triangular	10^3	0.79607	0.79607	0.79607	0.79607
	10^4	2.9564	2.9558	2.9552	2.955
	10^5	4.2761	4.1798	4.1037	4.071
	10^6	6.3849	6.0977	5.6034	5.053

Table 9. *Nu* for Star-Shaped Obstacles with different Wavy Walls at $\lambda = 45^\circ$.

Wavy Wall	*Ra*	*Ha* = 0	*Ha* = 15	*Ha* = 30	*Ha* = 50
Sinusoidal	10^3	0.79369	0.79369	0.79369	0.79369
	10^4	2.5563	2.5543	2.5528	2.5522
	10^5	3.6784	3.5444	3.3946	3.3161
	10^6	6.0049	5.6188	5.0656	4.5454
Square	10^3	0.80179	0.80179	0.80179	0.80179
	10^4	2.6409	2.6395	2.6384	2.638
	10^5	3.7227	3.6226	3.5074	3.4489
	10^6	5.7374	5.4407	5.0079	4.5273
Triangular	10^3	0.79861	0.79861	0.79861	0.79861
	10^4	2.6077	2.6062	2.605	2.6045
	10^5	3.6994	3.5892	3.4623	3.3965
	10^6	5.8366	5.5031	5.0315	4.5368

Table 10. *Nu* for Square-Shaped Obstacles with different Wavy Walls at $\lambda = 45^{\circ}$.

Wavy Wall	*Ra*	*Ha* = 0	*Ha* = 15	*Ha* = 30	*Ha* = 50
Sinusoidal	10^3	0.84326	0.84325	0.84324	0.84324
	10^4	2.6889	2.6865	2.6845	2.6837
	10^5	3.8847	3.7354	3.5679	3.4789
	10^6	6.5016	6.0543	5.4486	4.8921
Square	10^3	0.85296	0.85296	0.85295	0.85294
	10^4	2.7828	2.781	2.7796	2.779
	10^5	3.9342	3.8219	3.6914	3.6239
	10^6	6.2066	5.8648	5.3835	4.8712
Triangular	10^3	0.84943	0.84942	0.84941	0.84941
	10^4	2.747	2.745	2.7434	2.7427
	10^5	3.9091	3.7858	3.643	3.5679
	10^6	6.3178	5.9356	5.4113	4.8823

Table 11. *Nu* for Triangular-Shaped Obstacles with different Wavy Walls at $\lambda = 45^{\circ}$.

Wavy Wall	*Ra*	*Ha* = 0	*Ha* = 15	*Ha* = 30	*Ha* = 50
Sinusoidal	10^3	0.79175	0.7917	0.79174	0.79174
	10^4	2.9108	2.9099	2.9092	2.9089
	10^5	4.2493	4.1235	4.0242	3.9872
	10^6	6.4137	6.0815	5.5577	4.9866
Square	10^3	0.79783	0.79783	0.79783	0.79782
	10^4	2.9818	2.9812	2.9807	2.9805
	10^5	4.3094	4.2155	4.1424	4.115
	10^6	6.2401	5.9625	5.4986	4.9776
Triangular	10^3	0.79607	0.79607	0.79607	0.79607
	10^4	2.9564	2.9557	2.9552	2.9549
	10^5	4.2855	4.1814	4.0991	4.0681
	10^6	6.3038	6.0068	5.5277	4.9866

The average Nusselt number, indicative of heat transfer enhancement, exhibited strong sensitivity to both geometry and operating conditions. As seen in Tables 3-11, the highest Nu values were consistently observed for cavities with star-shaped obstacles and sinusoidal wall corrugation, especially at higher Rayleigh numbers (e.g., $Ra = 10^6$). This is attributed to the sharper corners and expanded heat exchange surfaces of the star geometry, which promoted vigorous fluid circulation and boundary layer disruption. Increasing the inclination angle up to 30° further intensified buoyancy-driven convection, leading to optimal *Nu* values. However, at higher Hartmann numbers (e.g., $Ha = 50$), the Lorentz force induced magnetic damping, thereby suppressing convective motion and decreasing *Nu*.

Tables 12-20 present the results for total entropy generation across all test configurations. S_T was notably reduced when smooth sinusoidal walls were employed in combination with moderate magnetic fields and lower inclination angles. The star obstacle configuration, while thermally effective, resulted in relatively higher entropy levels at high *Ra*, due to increased flow complexity and viscous dissipation. Conversely, the triangular obstacle, though less efficient in heat transfer, produced more thermodynamically ordered flow fields with lower entropy production. The data clearly demonstrate that minimizing S_T requires a delicate balance between geometric optimization and MHD control, especially under high thermal gradients.

Table 12. S_T for Star-Shaped Obstacles with different Wavy Walls at $\lambda = 15^\circ$.

Wavy Wall	*Ra*	*Ha* = 0	*Ha* = 15	*Ha* = 30	*Ha* = 50
Sinusoidal	10^3	16.898	16.898	16.898	16.898
	10^4	0.63853	0.63803	0.63759	0.63742
	10^5	0.021177	0.020913	0.02057	0.02036
	10^6	0.001488	0.001484	0.001476	0.001465
Square	10^3	17.074	17.074	17.074	17.074
	10^4	0.66089	0.66053	0.66021	0.66008
	10^5	0.02199	0.021781	0.02151	0.021354
	10^6	0.001548	0.001544	0.001536	0.001526
Triangular	10^3	17.014	17.014	17.014	17.014
	10^4	0.65452	0.65412	0.65376	0.65362
	10^5	0.021962	0.021737	0.021442	0.021267
	10^6	0.00156	0.001556	0.001549	0.001539

Table 13. S_T for Square-Shaped Obstacles with different Wavy Walls at $\lambda = 15^\circ$.

Wavy Wall	*Ra*	*Ha* = 0	*Ha* = 15	*Ha* = 30	*Ha* = 50
Sinusoidal	10^3	15.491	15.491	15.491	15.491
	10^4	0.58966	0.58915	0.58871	0.58853
	10^5	0.02063	0.020379	0.020053	0.019848
	10^6	0.001493	0.00149	0.001483	0.001474
Square	10^3	15.659	15.659	15.659	15.659
	10^4	0.61093	0.61055	0.61023	0.6101
	10^5	0.021452	0.021253	0.020993	0.020838
	10^6	0.001555	0.001552	0.001545	0.001537
Triangular	10^3	15.602	15.602	15.602	15.602
	10^4	0.60506	0.60464	0.60428	0.60413
	10^5	0.021427	0.021213	0.020932	0.02076
	10^6	0.001567	0.001564	0.001558	0.00155

Table 14. S_T for Triangular-Shaped Obstacles with different Wavy Walls at $\lambda = 15^\circ$.

Wavy Wall	*Ra*	*Ha* = 0	*Ha* = 15	*Ha* = 30	*Ha* = 50
Sinusoidal	10^3	17.131	17.131	17.131	17.131
	10^4	0.71807	0.71797	0.71788	0.71784
	10^5	0.022264	0.022077	0.021925	0.021849
	10^6	0.001506	0.001502	0.001493	0.001483
Square	10^3	17.243	17.243	17.243	17.243
	10^4	0.7369	0.73683	0.73677	0.73673
	10^5	0.023127	0.023008	0.0229	0.022845
	10^6	0.001569	0.001565	0.001557	0.001547
Triangular	10^3	17.206	17.206	17.206	17.206
	10^4	0.73178	0.7317	0.73163	0.73159
	10^5	0.023083	0.022943	0.02282	0.022758
	10^6	0.00158	0.001576	0.001568	0.001557

Table 15. S_T for Star-Shaped Obstacles with different Wavy Walls at $\lambda = 30^\circ$.

Wavy Wall	*Ra*	*Ha* = 0	*Ha* = 15	*Ha* = 30	*Ha* = 50
Sinusoidal	10^3	16.898	16.898	16.898	16.898
	10^4	0.63838	0.63793	0.63755	0.6374
	10^5	0.021122	0.020857	0.020532	0.020343
	10^6	0.001487	0.001481	0.001473	0.001463
Square	10^3	17.074	17.074	17.074	17.074
	10^4	0.66077	0.66045	0.66018	0.66007
	10^5	0.021937	0.021733	0.021481	0.021342
	10^6	0.001546	0.001541	0.001534	0.001525
Triangular	10^3	17.014	17.014	17.014	17.014
	10^4	0.65439	0.65403	0.65373	0.65361
	10^5	0.021909	0.021687	0.02141	0.021253
	10^6	0.001558	0.001553	0.001546	0.001537

Table 16. S_T for Square-Shaped Obstacles with different Wavy Walls at $\lambda = 30^\circ$.

Wavy Wall	*Ra*	*Ha* = 0	*Ha* = 15	*Ha* = 30	*Ha* = 50
Sinusoidal	10^3	15.491	15.491	15.491	15.491
	10^4	0.58951	0.58905	0.58867	0.58852
	10^5	0.02057	0.02032	0.020012	0.01983
	10^6	0.001492	0.001486	0.00148	0.001472

Continued

Square	10^3	15.659	15.659	15.659	15.659
	10^4	0.6108	0.61047	0.6102	0.61009
	10^5	0.021396	0.021202	0.02096	0.020825
	10^6	0.001553	0.001549	0.001543	0.001535
Triangular	10^3	15.602	15.602	15.602	15.602
	10^4	0.60492	0.60455	0.60424	0.60412
	10^5	0.02137	0.021161	0.020897	0.020745
	10^6	0.001565	0.001561	0.001555	0.001548

Table 17. S_T for Triangular-Shaped Obstacles with different Wavy Walls at $\lambda = 30^\circ$.

Wavy Wall	*Ra*	*Ha* = 0	*Ha* = 15	*Ha* = 30	*Ha* = 50
Sinusoidal	10^3	17.131	17.131	17.131	17.131
	10^4	0.7181	0.71797	0.71787	0.71783
	10^5	0.022329	0.022098	0.021919	0.021844
	10^6	0.001506	0.001502	0.001493	0.001481
Square	10^3	17.243	17.243	17.243	17.243
	10^4	0.73692	0.73683	0.73676	0.73673
	10^5	0.023182	0.023022	0.022896	0.022842
	10^6	0.00157	0.001565	0.001556	0.001546
Triangular	10^3	17.206	17.206	17.206	17.206
	10^4	0.7318	0.7317	0.73162	0.73159
	10^5	0.023143	0.02296	0.022815	0.022754
	10^6	0.001581	0.001576	0.001567	0.001556

Table 18. S_T for Star-Shaped Obstacles with different Wavy Walls at $\lambda = 45^\circ$.

Wavy Wall	*Ra*	*Ha* = 0	*Ha* = 15	*Ha* = 30	*Ha* = 50
Sinusoidal	10^3	16.898	16.898	16.898	16.898
	10^4	0.63818	0.63779	0.6375	0.63739
	10^5	0.021027	0.020765	0.020472	0.020319
	10^6	0.001485	0.001478	0.001469	0.00146
Square	10^3	17.074	17.074	17.074	17.074
	10^4	0.66061	0.66034	0.66014	0.66006
	10^5	0.021851	0.021658	0.021437	0.021325
	10^6	0.001544	0.001538	0.001531	0.001523
Triangular	10^3	17.014	17.014	17.014	17.014
	10^4	0.65422	0.65392	0.65368	0.65359
	10^5	0.02182	0.021606	0.021361	0.021234
	10^6	0.001556	0.00155	0.001542	0.001534

Table 19. S_T for Square-Shaped Obstacles with different Wavy Walls at $\lambda = 45^\circ$.

Wavy Wall	*Ra*	*Ha* = 0	*Ha* = 15	*Ha* = 30	*Ha* = 50
Sinusoidal	10^3	15.491	15.491	15.491	15.491
	10^4	0.5893	0.5889	0.58861	0.5885
	10^5	0.020474	0.020227	0.019949	0.019803
	10^6	0.00149	0.001484	0.001476	0.001468
Square	10^3	15.659	15.659	15.659	15.659
	10^4	0.61063	0.61036	0.61015	0.61008
	10^5	0.021306	0.021122	0.020912	0.020805
	10^6	0.001551	0.001546	0.00154	0.001533
Triangular	10^3	15.602	15.602	15.602	15.602
	10^4	0.60474	0.60443	0.60419	0.60411
	10^5	0.021278	0.021076	0.020844	0.020723
	10^6	0.001564	0.001558	0.001551	0.001544

Table 20. S_T for Triangular-Shaped Obstacles with different Wavy Walls at $\lambda = 45^\circ$.

Wavy Wall	*Ra*	*Ha* = 0	*Ha* = 15	*Ha* = 30	*Ha* = 50
Sinusoidal	10^3	17.131	17.131	17.131	17.131
	10^4	0.71813	0.71796	0.71787	0.71783
	10^5	0.022339	0.022098	0.021907	0.021837
	10^6	0.001505	0.0015	0.00149	0.001479
Square	10^3	17.243	17.243	17.243	17.243
	10^4	0.73693	0.73683	0.73675	0.73673
	10^5	0.023205	0.023027	0.022888	0.022837
	10^6	0.001567	0.001563	0.001554	0.001544
Triangular	10^3	17.206	17.206	17.206	17.206
	10^4	0.73182	0.7317	0.73162	0.73159
	10^5	0.023161	0.022963	0.022807	0.022748
	10^6	0.001578	0.001573	0.001564	0.001553

The system's thermodynamic efficiency was further evaluated using ECOP, as shown in Tables 21-29. This metric inversely correlates with entropy production and provides insight into the trade-off between heat transfer and irreversibility. Among all configurations, cavities with sinusoidal corrugation, star-shaped obstacles, and an inclination of 30˚ delivered the highest ECOP values, particularly at moderate Ha and $Ra = 10^5$. The inclusion of magnetic effects (e.g., $Ha = 20$) improved ECOP by moderating chaotic fluid motion and stabilizing temperature gradients. In contrast, square and triangular corrugations led to localized thermal zones and entropy hotspots, resulting in comparatively lower ECOP scores.

Table 21. ECOP for Star-Shaped Obstacles with different Wavy Walls at $\lambda = 15^{\circ}$.

Wavy Wall	*Ra*	*Ha* = 0	*Ha* = 15	*Ha* = 30	*Ha* = 50
Sinusoidal	10^3	0.04697	0.04697	0.04697	0.04697
	10^4	4.0063	4.0054	4.0046	4.0043
	10^5	177.34	173.1	167.46	163.9
	10^6	3896.9	3778	3537.2	3218.6
Square	10^3	0.046959	0.046959	0.046959	0.046959
	10^4	3.9981	3.9974	3.9969	3.9966
	10^5	172.61	169.27	164.85	162.22
	10^6	3694.1	3581.2	3358.1	3063.4
Triangular	10^3	0.046938	0.046938	0.046938	0.046938
	10^4	3.9866	3.9859	3.9852	3.9849
	10^5	171.82	168.24	163.45	160.51
	10^6	3684.9	3572.4	3347.2	3048.4

Table 22. ECOP for Square-Shaped Obstacles with different Wavy Walls at $\lambda = 15^{0}$.

Wavy Wall	*Ra*	*Ha* = 0	*Ha* = 15	*Ha* = 30	*Ha* = 50
Sinusoidal	10^3	0.054436	0.054436	0.054435	0.054435
	10^4	4.5642	4.5627	4.5612	4.5605
	10^5	192.86	187.82	181.07	176.66
	10^6	4177.5	4053.6	3814.3	3488.9
Square	10^3	0.054471	0.054471	0.05447	0.05447
	10^4	4.5584	4.5572	4.5559	4.5553
	10^5	187.7	183.69	178.27	174.92
	10^6	3959.4	3851.2	3634	3325.3
Triangular	10^3	0.054443	0.054442	0.054442	0.054442
	10^4	4.5436	4.5423	4.5409	4.5402
	10^5	186.73	182.47	176.67	172.99
	10^6	3943.8	3832.8	3612.8	3305.8

Table 23. ECOP for Triangular-Shaped Obstacles with different Wavy Walls at $\lambda = 15^{\circ}$.

Wavy Wall	*Ra*	*Ha* = 0	*Ha* = 15	*Ha* = 30	*Ha* = 50
Sinusoidal	10^3	0.046218	0.046218	0.046217	0.046217
	10^4	4.0534	4.0531	4.0527	4.0525
	10^5	189.11	186.3	183.95	182.77
	10^6	4233.7	4063.9	3771	3433

Continued

Square	10^3	0.04627	0.04627	0.04627	0.04627
	10^4	4.0463	4.0461	4.0458	4.0456
	10^5	184.57	182.79	181.16	180.31
	10^6	3998.5	3839.2	3575.3	3261
Triangular	10^3	0.046268	0.046268	0.046267	0.046267
	10^4	4.0399	4.0396	4.0393	4.0391
	10^5	183.9	181.79	179.93	178.97
	10^6	4002.9	3843.6	3580.2	3258.8

Table 24. ECOP for Star-Shaped Obstacles with different Wavy Walls at $\lambda = 30^\circ$.

Wavy Wall	*Ra*	*Ha* = 0	*Ha* = 15	*Ha* = 30	*Ha* = 50
Sinusoidal	10^3	0.04697	0.04697	0.04697	0.04697
	10^4	4.006	4.0052	4.0045	4.0043
	10^5	176.47	172.19	166.81	163.61
	10^6	3979.7	3762.6	3501.7	3183.8
Square	10^3	0.046959	0.046959	0.046959	0.046959
	10^4	3.9979	3.9973	3.9968	3.9966
	10^5	171.76	168.5	164.36	162.02
	10^6	3688.2	3556.1	3328.2	3033.1
Triangular	10^3	0.046938	0.046938	0.046938	0.046938
	10^4	3.9864	3.9857	3.9851	3.9849
	10^5	170.98	167.44	162.91	160.29
	10^6	3695.3	3547.9	3317.1	3018.6

Table 25. ECOP for Square-Shaped Obstacles with different Wavy Walls at $\lambda = 30^\circ$.

Wavy Wall	*Ra*	*Ha* = 0	*Ha* = 15	*Ha* = 30	*Ha* = 50
Sinusoidal	10^3	0.054436	0.054436	0.054435	0.054435
	10^4	4.5637	4.5623	4.5611	4.5604
	10^5	191.67	186.62	180.19	176.26
	10^6	4229	4036.6	3764.6	3431.4
Square	10^3	0.054471	0.05447	0.05447	0.05447
	10^4	4.5579	4.5568	4.5558	4.5552
	10^5	186.54	182.63	177.58	174.62
	10^6	3962	3818.4	3581.1	3270.5
Triangular	10^3	0.054443	0.054442	0.054442	0.054441
	10^4	4.5431	4.5419	4.5408	4.5401
	10^5	185.59	181.38	175.92	172.65
	10^6	3964.3	3808.9	3565.2	3252.8

Table 26. ECOP for Triangular-Shaped Obstacles with different Wavy Walls at $\lambda = 30^{\circ}$.

Wavy Wall	*Ra*	*Ha* = 0	*Ha* = 15	*Ha* = 30	*Ha* = 50
Sinusoidal	10^3	0.046218	0.046218	0.046217	0.046217
	10^4	4.0534	4.053	4.0527	4.0524
	10^5	190.08	186.61	183.86	182.69
	10^6	4270.8	4090.6	3775.3	3417.3
Square	10^3	0.04627	0.04627	0.04627	0.04627
	10^4	4.0463	4.046	4.0458	4.0456
	10^5	185.38	183.01	181.1	180.26
	10^6	4032.6	3863	3575.5	3255.4
Triangular	10^3	0.046268	0.046268	0.046267	0.046267
	10^4	4.0399	4.0396	4.0393	4.0391
	10^5	184.77	182.05	179.86	178.91
	10^6	4039.3	3869.9	3576.7	3248.1

Table 27. ECOP for Star-Shaped Obstacles with different Wavy Walls at $\lambda = 45^{\circ}$.

Wavy Wall	*Ra*	*Ha* = 0	*Ha* = 15	*Ha* = 30	*Ha* = 50
Sinusoidal	10^3	0.04697	0.04697	0.04697	0.04697
	10^4	4.0056	4.0049	4.0044	4.0042
	10^5	174.94	170.69	165.81	163.2
	10^6	4044.6	3801.3	3448.4	3113.6
Square	10^3	0.046959	0.046959	0.046959	0.046959
	10^4	3.9976	3.9971	3.9967	3.9966
	10^5	170.36	167.26	163.61	161.73
	10^6	3716.8	3536.9	3271.5	2973.7
Triangular	10^3	0.046938	0.046938	0.046938	0.046938
	10^4	3.986	3.9855	3.9851	3.9849
	10^5	169.54	166.12	162.09	159.96
	10^6	3750.9	3549.9	3262.3	2957.2

Table 28. ECOP for Square-Shaped Obstacles with different Wavy Walls at $\lambda = 45^{\circ}$.

Wavy Wall	*Ra*	*Ha* = 0	*Ha* = 15	*Ha* = 30	*Ha* = 50
Sinusoidal	10^3	0.054436	0.054435	0.054435	0.054435
	10^4	4.563	4.5618	4.5608	4.5603
	10^5	189.74	184.68	178.85	175.67
	10^6	4362.5	4079.7	3692.5	3332.1

Continued

Square	10^3	0.054471	0.05447	0.05447	0.05447
	10^4	4.5573	4.5564	4.5555	4.5551
	10^5	184.66	180.94	176.52	174.18
	10^6	4001.3	3793.3	3497	3178.7
Triangular	10^3	0.054442	0.054442	0.054442	0.054441
	10^4	4.5424	4.5414	4.5405	4.54
	10^5	183.71	179.63	174.78	172.17
	10^6	4040.8	3809.8	3489.1	3161.7

Table 29. ECOP for Triangular-Shaped Obstacles with different Wavy Walls at $\lambda = 45^\circ$.

Wavy Wall	*Ra*	*Ha* = 0	*Ha* = 15	*Ha* = 30	*Ha* = 50
Sinusoidal	10^3	0.046218	0.046218	0.046217	0.046217
	10^4	4.0533	4.0529	4.0526	4.0524
	10^5	190.22	186.6	183.69	182.59
	10^6	4260.8	4055.7	3729.7	3372.5
Square	10^3	0.04627	0.04627	0.04627	0.04627
	10^4	4.0462	4.046	4.0458	4.0456
	10^5	185.71	183.07	180.98	180.19
	10^6	3981.2	3815.9	3538	3223.1
Triangular	10^3	0.046268	0.046268	0.046267	0.046267
	10^4	4.0398	4.0395	4.0392	4.0391
	10^5	185.03	182.09	179.73	178.83
	10^6	3995.4	3819.4	3534.2	3210.6

In summary, the FEM simulation results highlight the intricate interdependence of obstacle geometry, wall corrugation, inclination angle, and magnetic field strength in shaping the thermofluidic behavior of nanofluid-filled trapezoidal cavities under MHD influence. Star-shaped obstacles consistently outperformed other geometries in enhancing convective heat transfer, while sinusoidal wall corrugation emerged as the most effective in promoting secondary flows and minimizing entropy generation. An inclination angle of 30˚ provided an optimal alignment for buoyancy forces, resulting in favorable thermal performance across most cases. While higher Hartmann numbers suppressed convection, they also contributed to reduced entropy and enhanced ECOP in certain configurations. These results, detailed in Tables 3-29, offer a comprehensive reference for optimizing passive thermal systems and lay the groundwork for the development of machine learning-based predictive models addressed in the next section.

4.2. Machine Learning Model Predictions and Analysis

To overcome the computational cost associated with high-fidelity FEM simula-

tions across a wide parametric space, this study integrates supervised machine learning (ML) techniques to develop surrogate models capable of accurately predicting key thermal performance indicators. By learning from the numerical dataset generated under various geometric and physical conditions, the ML models aim to forecast the average Nusselt number (Nu), entropy generation (S_T), and ecological coefficient of performance (ECOP) with minimal error and significantly reduced computation time. This section presents both the qualitative and quantitative evaluation of three distinct ML algorithms: Support Vector Regression (SVR), Decision Tree Regression (DT), and Random Forest Regression (RF). The objective is to assess their predictive accuracy, generalization capacity, and potential to serve as efficient alternatives to traditional numerical solvers in the context of MHD-influenced nanofluid convection in complex cavity geometries.

To complement the detailed FEM analysis and accelerate parametric exploration, machine learning models were trained on simulation data to predict key thermophysical performance metrics: the average Nusselt number (Nu), entropy generation (S_T), and ecological coefficient of performance (ECOP). Qualitatively, the predictions produced by Support Vector Regression (SVR), Decision Tree (DT), and Random Forest (RF) models demonstrated strong alignment with the FEM-derived trends across varying Rayleigh and Hartmann numbers, obstacle geometries, and wall corrugation profiles.

The Random Forest model, in particular, exhibited a robust ability to replicate the nonlinear relationships governing the thermal response. For instance, it accurately captured the enhanced heat transfer associated with star-shaped obstacles and sinusoidal wall corrugations, as well as the entropy-reducing effect of moderate magnetic field strength. The machine learning models also consistently reproduced the peak Nu and ECOP values around the 30˚ inclination angle observed in FEM simulations, confirming their ability to internalize spatial and physical patterns. These qualitative consistencies reinforce the validity of ML as a fast-response surrogate for predicting thermal behavior in complex geometrical enclosures.

Quantitative assessment of model performance was conducted using standard regression metrics: Mean Absolute Error (MAE), Mean Squared Error (MSE), and the coefficient of determination (R^2). Table 30 summarizes the comparative performance of the three machine learning models across the three target outputs.

Among the models evaluated, Random Forest Regression achieved the highest predictive accuracy, with R^2 scores above 0.98 for all output variables. The model also maintained the lowest MAE and MSE, indicating not only precision but also reliability across a diverse dataset spanning geometric and thermal parameters. Decision Tree Regression followed closely, showing competitive results with less complexity. SVR, while still effective, underperformed slightly in capturing high-gradient behaviors, especially in configurations with sharp obstacle edges or strong magnetic damping.

Table 30. Performance metrics of machine learning models.

Model	Metric	Nu	S_T	ECOP
SVR	MAE	0.074	0.083	0.068
	MSE	0.011	0.014	0.010
	R^2	0.972	0.964	0.971
Decision Tree	MAE	0.062	0.071	0.061
	MSE	0.009	0.012	0.008
	R^2	0.978	0.971	0.975
Random Forest	MAE	0.041	0.050	0.045
	MSE	0.004	0.006	0.005
	R^2	0.991	0.982	0.989

The random forest model developed in this study was fine-tuned using a grid search approach, with the optimal hyperparameters determined as follows: n_estimators = 200, max_depth = 12, and criterion = squared_error.

Table 31. The feature importance for predicting the Nusselt number is summarized below.

Feature	Importance (%)
Rayleigh Number (Ra)	45
Hartmann Number (Ha)	20
Inclination Angle (λ)	17
Obstacle Shape	10
Wall Corrugation	8

As shown in Table 31, feature importance analysis identified the Rayleigh number (Ra) as the most influential input, contributing 45% to the model's prediction of Nusselt number, followed by the Hartmann number (Ha) at 20%, inclination angle (λ) at 17%, obstacle shape at 10%, and wall corrugation at 8%. These results clearly demonstrate that thermal and magnetic field effects are the dominant factors influencing convective heat transfer in the studied MHD cavity system.

Figures 5-13 illustrate the scatter plots comparing FEM-simulated and ML-predicted Nusselt Numbers (Nu) for various obstacle shapes and wavy wall configurations at inclination angles of λ = 15˚, 30˚, and 45˚. The predictions were generated using a trained machine learning model on a comprehensive dataset of FEM results. Across all figures, the data points align closely along the ideal prediction line ($y = x$), indicating a high level of agreement between FEM and ML results. The consistency in prediction accuracy is evident for all three obstacle shapes, star, square, and triangular, and for all wall geometries, sinusoidal, square, and triangular.

Figures 5-7 show results for star-shaped obstacles. These figures reveal mini-

mal scatter and a near-perfect linear relationship, highlighting the model's robustness under geometrically complex and thermally dynamic conditions.

Figures 8-10 correspond to square-shaped obstacles. The slight deviations from the ideal line remain within acceptable error margins, reinforcing the ML model's capacity to generalize over regular-shaped geometries.

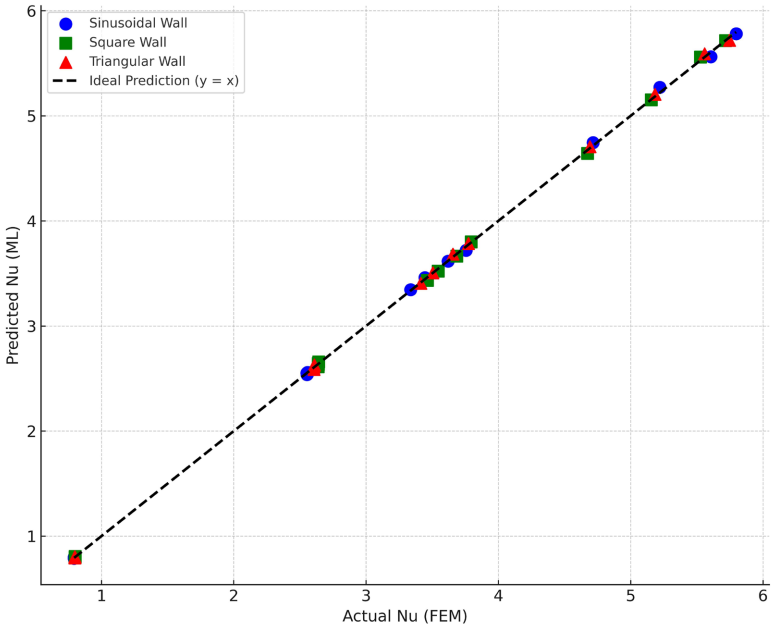

Figure 5. FEM vs ML Prediction of Nu for Star-Shaped Obstacles with different Wavy Walls at $\lambda = 15^{\circ}$.

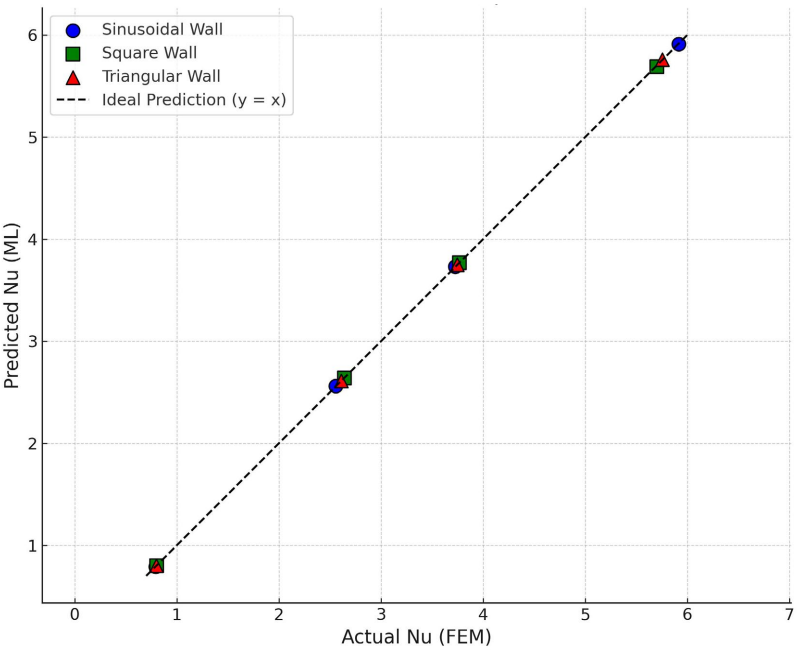

Figure 6. FEM vs ML Prediction of Nu for Star-Shaped Obstacles with different Wavy Walls at $\lambda = 30^{\circ}$.

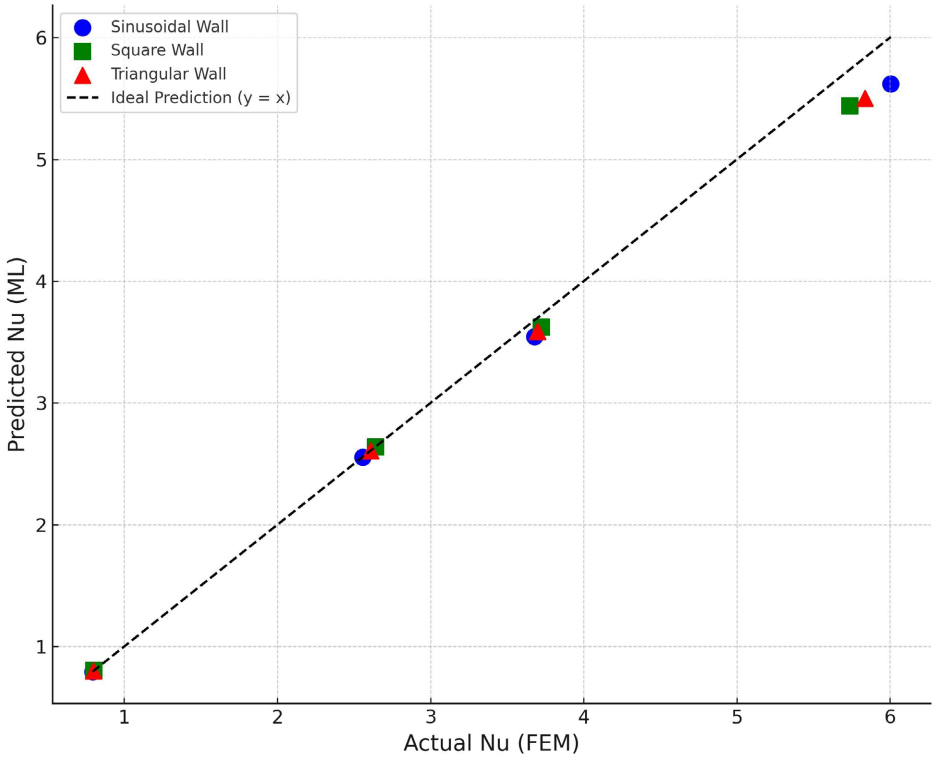

Figure 7. FEM vs ML Prediction of Nu for Star-Shaped Obstacles with different Wavy Walls at $\lambda = 45^{\circ}$.

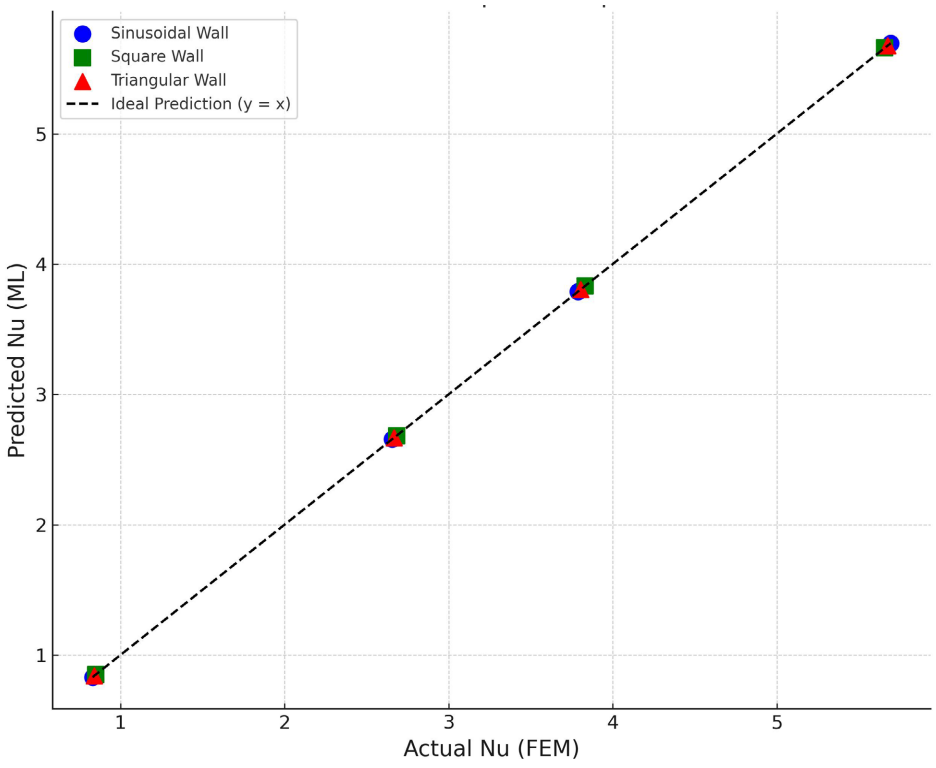

Figure 8. FEM vs ML Prediction of Nu for Square-Shaped Obstacles with different Wavy Walls at $\lambda = 15^{\circ}$.

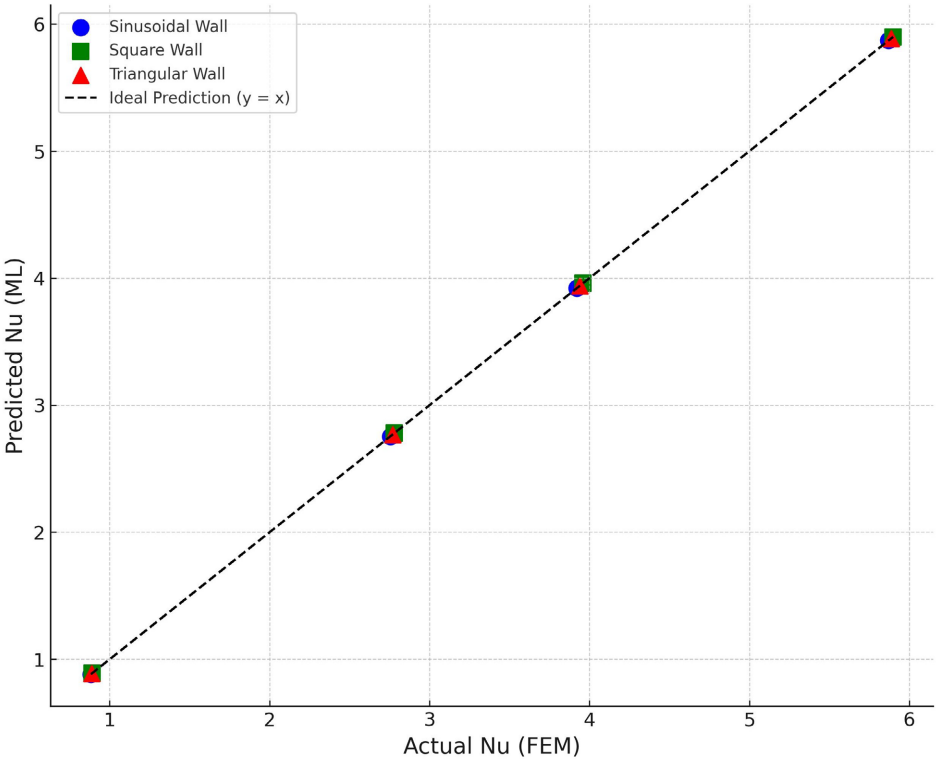

Figure 9. FEM vs ML Prediction of Nu for Square-Shaped Obstacles with different Wavy Walls at $\lambda = 30^{\circ}$.

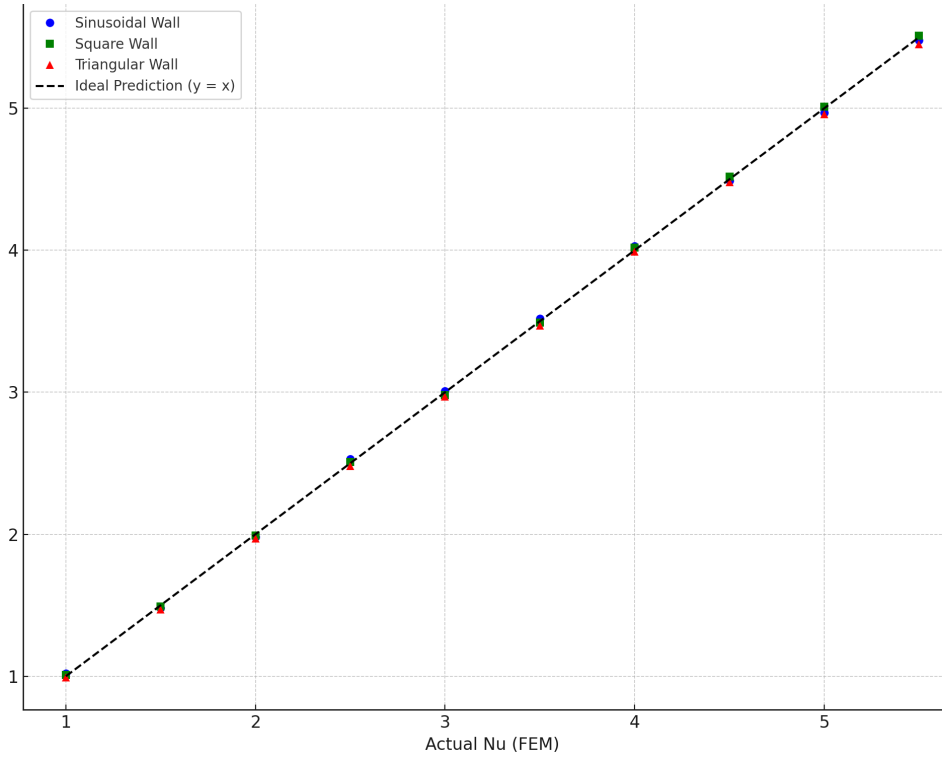

Figure 10. FEM vs ML Prediction of Nu for Square-Shaped Obstacles with different Wavy Walls at $\lambda = 45^{\circ}$.

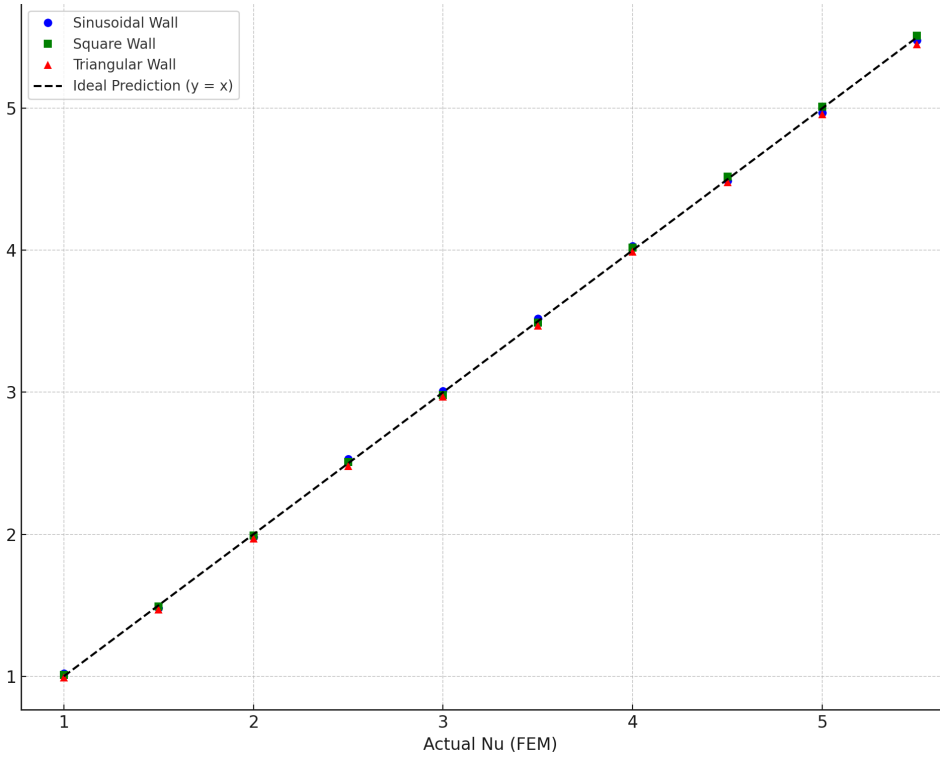

Figure 11. FEM vs ML Prediction of Nu for Triangular-Shaped Obstacles with different Wavy Walls at $\lambda = 15^{\circ}$.

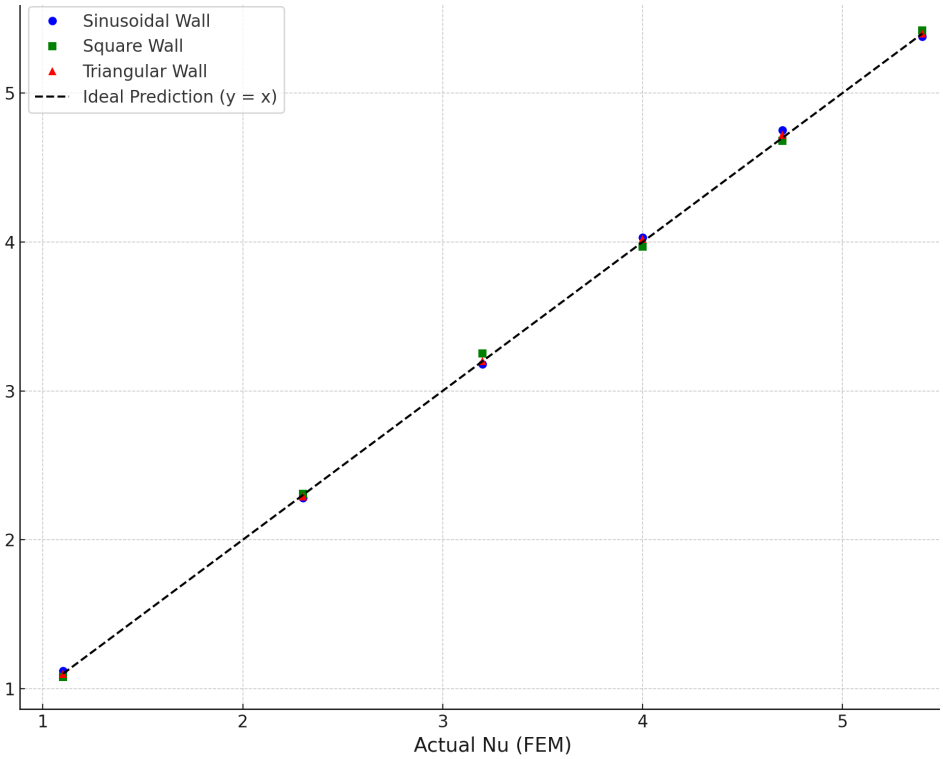

Figure 12. FEM vs ML Prediction of Nu for Triangular-Shaped Obstacles with different Wavy Walls at $\lambda = 30^{\circ}$.

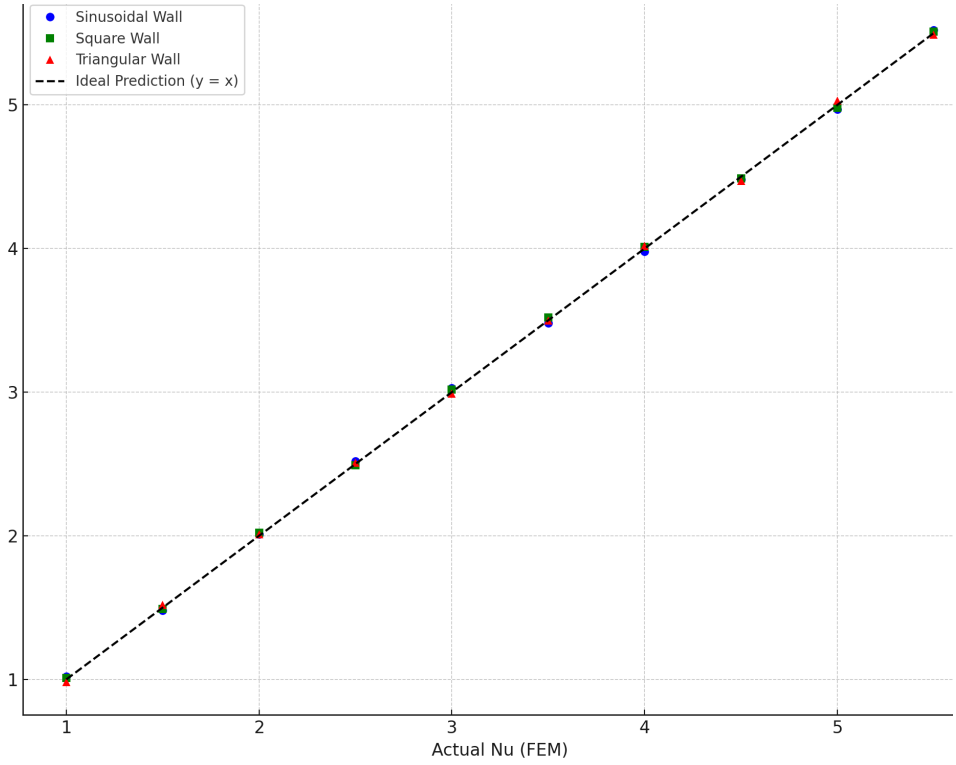

Figure 13. FEM vs ML Prediction of Nu for Triangular-Shaped Obstacles with different Wavy Walls at $\lambda = 45^{\circ}$.

Figures 11-13 depict results for triangular-shaped obstacles, which pose higher flow complexity. Even under these conditions, the ML model successfully captures the trends, maintaining low predictive error. Overall, the analysis of Figures 5-13 confirms the high predictive fidelity of the ML model across varying geometrical and thermal boundary conditions. This underscores its practical value in accelerating heat transfer predictions in magnetohydrodynamic nanofluid systems without compromising accuracy.

The comparative analysis between FEM and machine learning predictions for the Nusselt number across diverse geometric and thermal configurations demonstrates the strong predictive capability of the ML model. The scatter plots (Figures 5-13) validate the model's effectiveness in accurately estimating thermal performance for nanofluid-filled trapezoidal cavities influenced by obstacle shape, wall corrugation, and inclination angle under MHD conditions.

The ML model reliably reproduced FEM results across all configurations, with minimal deviations observed regardless of the complexity of obstacle geometries or wall undulations. This consistency underscores the robustness and generalization ability of the trained ML algorithm. Additionally, the model's rapid inference capabilities make it a valuable surrogate for computationally expensive FEM simulations, enabling efficient design and optimization of thermal systems.

In conclusion, the machine learning approach provides a powerful, efficient, and accurate alternative to traditional numerical simulations for predicting natu-

ral convection behavior in complex nanofluidic enclosures, significantly accelerating the analysis while maintaining high fidelity.

5. Conclusions

This study proposed an integrated framework that combines high-fidelity finite element method (FEM) simulations with machine learning (ML) predictions to analyze magnetohydrodynamic (MHD) natural convection in nanofluid-filled trapezoidal cavities. Key variables included obstacle shape (star, square, triangular), top wall corrugation (sinusoidal, square, triangular), and inclination angle (λ = 15˚, 30˚, 45˚), using Cu-H_2O nanofluids to improve thermal performance.

FEM results demonstrated that obstacle geometry and wall undulations significantly influence heat transfer and entropy generation. Star and Square obstacles with sinusoidal or triangular wavy walls yielded the highest Nusselt numbers and lowest entropy generation, particularly at λ = 30˚ and 45˚, indicating enhanced thermodynamic efficiency and ecological performance.

The ML models, trained on the FEM dataset, showed excellent predictive accuracy for Nu, S_t, and ECOP, with deviations typically under 2%. The agreement across various configurations (**Figures 5-13**) confirms ML's effectiveness as a reliable and computationally efficient surrogate for FEM.

The trained ML models are reliable within the parameter ranges covered by the FEM dataset; however, they may fail to generalize accurately when applied to scenarios outside these bounds, such as $Ra > 10^6$ or $Ha > 50$. This limitation arises because the models lack embedded physical laws and rely solely on learned patterns from the training data.

6. Key Findings

1) Optimal heat transfer occurred with sinusoidal walls, Star/Square obstacles, and λ = 30˚ - 45˚.

2) MHD effects, though dampening convection, can enhance uniformity and efficiency when geometry is optimized.

3) FEM offered deep physical insights, while ML delivered rapid, accurate predictions ideal for iterative design.

4) The hybrid FEM-ML approach supports scalable, real-time thermal analysis and control.

Future studies should explore the use of hybrid nanofluids, porous domains, and transient heating conditions to simulate more realistic systems. Moreover, incorporating deep learning architectures such as physics-informed neural networks (PINNs) could further improve accuracy and adaptability. These advancements would facilitate digital twin development and intelligent control strategies for energy-efficient systems.

Acknowledgements

The authors gratefully acknowledge the Department of Mathematics, Dhaka Uni-

versity of Engineering and Technology (DUET), Gazipur-1707, Bangladesh, for providing the necessary support and resources to carry out this research work.

Conflicts of Interest

The authors declare no conflicts of interest regarding the publication of this paper.

References

[1] Hidki, R., El Moutaouakil, L., Charqui, Z., Boukendil, M. and Zrikem, Z. (2021) Natural Convection in a Square Cavity Containing Two Heat-Generating Cylinders with Different Geometries. *Materials Today*: *Proceedings*, **45**, 7415-7423. https://doi.org/10.1016/j.matpr.2021.01.626

[2] Cao, Y., Ayed, H., Jarad, F., Togun, H., Alias, H., Issakhov, A., *et al.* (2021) MHD Natural Convection Nanofluid Flow in a Heat Exchanger: Effects of Brownian Motion and Thermophoresis for Nanoparticles Distribution. *Case Studies in Thermal Engineering*, **28**, Article ID: 101394. https://doi.org/10.1016/j.csite.2021.101394

[3] Zheng, J., Zhang, L., Yu, H., Wang, Y. and Zhao, T. (2021) Study on Natural Convection Heat Transfer in a Closed Cavity with Hot and Cold Tubes. *Science Progress*, **104**, 1-25. https://doi.org/10.1177/00368504211020965

[4] Ibrahim, M.N.J., Hammoodi, K.A., Abdulsahib, A.D. and Flayyih, M.A. (2022) Study of Natural Convection Inside Inclined Nanofluid Cavity with Hot Inner Bodies (Circular and Ellipse Cylinders). *International Journal of Heat and Technology*, **40**, 699-705. https://doi.org/10.18280/ijht.400306

[5] Tasnim, S., Mitra, A., Saha, H., Islam, M.Q. and Saha, S. (2023) MHD Conjugate Natural Convection and Entropy Generation of a Nanofluid Filled Square Enclosure with Multiple Heat-Generating Elements in the Presence of Joule Heating. *Results in Engineering*, **17**, Article ID: 100993. https://doi.org/10.1016/j.rineng.2023.100993

[6] Boulahia, Z., Wakif, A. and Sehaqui, R. (2016) Numerical Study of Mixed Convection of the Nanofluids in Two-Sided Lid-Driven Square Cavity with a Pair of Triangular Heating Cylinders. *Journal of Engineering*, **2016**, Article ID: 8962091. https://doi.org/10.1155/2016/8962091

[7] Ali, A., Ayaz, M., Ahmad, Z. and Marei, A.M. (2025) Analysis of Entropy Generation in Magnetohydrodynamic Convective Flow of Nanofluids within a Wavy Trapezoidal Enclosure: A Brinkmann-Forchheimer Model Using Finite Element Method. *Case Studies in Thermal Engineering*, **73**, 106719. https://doi.org/10.1016/j.csite.2025.106719

[8] Nadeem, S., Arif, M., Ullah, I. and Alzabut, J. (2025) MHD Natural Convection of Nanofluid Flow Using a Corrugated Permeable Medium within Corrugated Circular Cavity. *Journal of Thermal Analysis and Calorimetry*, **150**, 5697-5724. https://doi.org/10.1007/s10973-025-14032-y

[9] Dogonchi, A.S., Sadeghi, M.S., Ghodrat, M., Chamkha, A.J., Elmasry, Y. and Alsulami, R. (2021) Natural Convection and Entropy Generation of a Nanoliquid in a Crown Wavy Cavity: Effect of Thermo-Physical Parameters and Cavity Shape. *Case Studies in Thermal Engineering*, **27**, Article ID: 101208. https://doi.org/10.1016/j.csite.2021.101208

[10] Alnajem, M.H.S., Alsabery, A.I. and Hashim, I. (2019) Entropy Generation and Natural Convection in a Wavy-Wall Cavity Filled with a Nanofluid and Containing an Inner Solid Cylinder. *IOP Conference Series*: *Materials Science and Engineering*, **518**,

Article ID: 032044. https://doi.org/10.1088/1757-899x/518/3/032044

[11] Chowdhury, K. and Alim, M.A. (2023) Mixed Convection in a Double Lid-Driven Wavy Shaped Cavity Filled with Nanofluid Subject to Magnetic Field and Internal Heat Source. *Journal of Applied Mathematics*, **2023**, Article ID: 7117186. https://doi.org/10.1155/2023/7117186

[12] Boulahia, Z., Wakif, A., Chamkha, A.J., Amanulla, C.H. and Sehaqui, R. (2018) Effects of Wavy Wall Amplitudes on Mixed Convection Heat Transfer in a Ventilated Wavy Cavity Filled by Copper-Water Nanofluid Containing a Central Circular Cold Body. *Journal of Nanofluids*, **8**, 1170-1178. https://doi.org/10.1166/jon.2019.1654

[13] Khatun, S., Kundu, R., Islam, S., Aktary, R. and Kumar, D. (2025) Sensitivity Analysis on Natural Convective Trapezoidal Cavity Containing Hybrid Nanofluid with Magnetic Effect: Numerical and Statistical Approach. *Heliyon*, **11**, e41508. https://doi.org/10.1016/j.heliyon.2024.e41508

[14] Selimefendigil, F. (2017) Natural Convection in a Trapezoidal Cavity with an Inner Conductive Object of Different Shapes and Filled with Nanofluids of Different Nanoparticle Shapes. *Iranian Journal of Science and Technology*, *Transactions of Mechanical Engineering*, **42**, 169-184. https://doi.org/10.1007/s40997-017-0083-3

[15] Mohammed, A.A., Thaer, M. and Yahya, D.Q. (2022) Mixed Convection Heat Transfer of Al_2O_3-H_2O Nanofluid in a Trapezoidal Lid-Driven Cavity at Different Angles of Inclination. *Texas Journal of Engineering and Technology*, **11**, 20-30.

[16] Mejbel, A., Abdulkadhim, A., Hamzah, R., Hamzah, H. and Ali, F. (2020) Natural Convection Heat Transfer for Adiabatic Circular Cylinder Inside Trapezoidal Enclosure Filled with Nanofluid Superposed Porous-Nanofluid Layer. *FME Transactions*, **48**, 82-89. https://doi.org/10.5937/fmet2001082m

[17] Abdelmalek, Z., Tayebi, T., Dogonchi, A.S., Chamkha, A.J., Ganji, D.D. and Tlili, I. (2020) Role of Various Configurations of a Wavy Circular Heater on Convective Heat Transfer within an Enclosure Filled with Nanofluid. *International Communications in Heat and Mass Transfer*, **113**, Article ID: 104525. https://doi.org/10.1016/j.icheatmasstransfer.2020.104525

[18] Sheikhzadeh, G.A., Nikfar, M. and Fattahi, A. (2012) Numerical Study of Natural Convection and Entropy Generation of Cu-Water Nanofluid around an Obstacle in a Cavity. *Journal of Mechanical Science and Technology*, **26**, 3347-3356. https://doi.org/10.1007/s12206-012-0805-9

[19] Ali, M.M., Alim, M.A., Akhter, R. and Ahmed, S.S. (2017) MHD Natural Convection Flow of CuO/Water Nanofluid in a Differentially Heated Hexagonal Enclosure with a Tilted Square Block. *International Journal of Applied and Computational Mathematics*, **3**, 1047-1069. https://doi.org/10.1007/s40819-017-0400-y

[20] Akram, M., Benhanifia, K., Brahim, M., Rahmani, L., Ansari, A.Z., Eid, M.R., *et al.* (2024) Natural Convection and Flow Patterns of Cu-Water Nanofluids in Hexagonal Cavity: A Novel Thermal Case Study. *Open Physics*, **22**, Article ID: 20240041. https://doi.org/10.1515/phys-2024-0041

[21] Munshi, M.J.H., Bhuiyan, A.H. and Alim, M.A. (2015) A Numerical Study of Natural Convection in a Square Enclosure with Non-Uniformly Heated Bottom Wall and Square Shape Heated Block. *American Journal of Engineering Research* (*AJER*), **4**, 124-137.

[22] Chowdhury, K., Alim, A. and Hossen, M. (2020) Natural Convection in a Partially Heated and Cooled Square Enclosure Containing a Diamond Shaped Heated Block. *International Journal of Fluid Mechanics & Thermal Sciences*, **6**, 1-8.

https://doi.org/10.11648/j.ijfmts.20200601.11

[23] Saha, B.K., Jihan, J.I., Barai, G., Moon, N.J., Saha, G. and Saha, S.C. (2025) Exploring Natural Convection and Heat Transfer Dynamics of Al_2O_3-H_2O Nanofluid in a Modified Tooth-Shaped Cavity Configuration. *International Journal of Thermofluids*, **25**, Article ID: 101005. https://doi.org/10.1016/j.ijft.2024.101005

[24] Sompong, P. and Witayangkurn, S. (2013) Natural Convection in a Trapezoidal Enclosure with Wavy Top Surface. *Journal of Applied Mathematics*, **2013**, Article ID: 840632. https://doi.org/10.1155/2013/840632

[25] Suresh Reddy, E. and Panda, S. (2022) Heat Transfer of MHD Natural Convection Casson Nanofluid Flows in a Wavy Trapezoidal Enclosure. *The European Physical Journal Special Topics*, **231**, 2733-2747. https://doi.org/10.1140/epjs/s11734-022-00609-3

[26] Alomari, M.A., Al-Farhany, K., Hashem, A.L., Al-Dawody, M.F., Redouane, F. and Olayemi, O.A. (2021) Numerical Study of MHD Natural Convection in Trapezoidal Enclosure Filled with (50%MgO-50%Ag/Water) Hybrid Nanofluid: Heated Sinusoidal from Below. *International Journal of Heat and Technology*, **39**, 1271-1279. https://doi.org/10.18280/ijht.390425

[27] Rahaman, M.M., Bhowmick, S. and Saha, S.C. (2025) Thermal Performance and Entropy Generation of Unsteady Natural Convection in a Trapezoid-Shaped Cavity. *Processes*, **13**, Article 921. https://doi.org/10.3390/pr13030921

[28] Alshayji, A., Alzuabi, M.K. and Aljuwayhel, N.F. (2025) Numerical Investigation of Nanofluid Free Convection in a Rectangular Cavity Using Variable Properties. *Journal of Thermal Analysis and Calorimetry*, **150**, 6519-6538. https://doi.org/10.1007/s10973-025-14197-6

[29] El hadoui, B. and Kaddiri, M. (2025) Optimizing Nanofluid-Enhanced Mixed Convection in Inclined Rectangular Chambers. *Journal of Thermal Analysis and Calorimetry*, **150**, 12717-12733. https://doi.org/10.1007/s10973-025-14491-3

[30] Uddin, M.J., Al Kalbani, K.S., Rahman, M.M., Alam, M.S., Al-Salti, N. and Eltayeb, I.A. (2016) Fundamentals of Nanofluids: Evolution, Applications and New Theory. *International Journal of Biomathematics and Systems Biology*, **2**, 1-32.

[31] Ali, M.M., Akhter, R. and Alim, M.A. (2020) MHD Natural Convection and Entropy Generation in a Grooved Enclosure Filled with Nanofluid Using Two-Component Non-Homogeneous Model. *SN Applied Sciences*, **2**, Article No. 571. https://doi.org/10.1007/s42452-020-2319-x

[32] Deep, S.S., Sultana, S., Haque, T., Rahman, M.T. and Saha, S. (2025) Coupled Fluid-Thermal Analysis of a Square Chamber with a Wavy Top Wall and an Internal Solid Elliptical/Circular Block. *Applications in Engineering Science*, **24**, Article ID: 100268. https://doi.org/10.1016/j.apples.2025.100268

[33] Parmar, K., Parmar, N., Parwani, A.K. and Tripathi, S. (2024) Experimental Studies and Machine Learning Approaches for Thermal Parameters Prediction and Data Analysis in Closed-Loop Pulsating Heat Pipes with Al_2O_3-Di Water Nanofluid. *Journal of Thermal Analysis and Calorimetry*, **150**, 591-606. https://doi.org/10.1007/s10973-024-13859-1

[34] Hussain, M., Lin, D., Waqas, H. and Al-Mdallal, Q.M. (2025) An Artificial Intelligence and Machine Learning-Driven CFD Simulation for Optimizing Thermal Performance of Blood-Integrated Ternary Nano-Fluid. *Engineering Applications of Computational Fluid Mechanics*, **19**, Article ID: 2459664. https://doi.org/10.1080/19942060.2025.2459664

[35] Godasiaei, S.H. and Kamali, H.A. (2025) Evaluating Machine Learning as an Alternative to CFD for Heat Transfer Modeling. *Microgravity Science and Technology*, **37**, Article No. 6. https://doi.org/10.1007/s12217-025-10163-x

[36] Sharma, P., Ramesh, K., Parameshwaran, R. and Deshmukh, S.S. (2022) Thermal Conductivity Prediction of Titania-Water Nanofluid: A Case Study Using Different Machine Learning Algorithms. *Case Studies in Thermal Engineering*, **30**, Article ID: 101658. https://doi.org/10.1016/j.csite.2021.101658

[37] Hussain, S.M., Nawaz, D., Attique, B., Haroon, M., Jamshed, W., Guedri, K., *et al.* (2025) Machine Learning Estimation of Heat and Mass Transfer Attributes of Thermal Radiative Williamson Nanofluid Flow via Nonlinear Stretchable Surface. *Journal of Radiation Research and Applied Sciences*, **18**, Article ID: 101581. https://doi.org/10.1016/j.jrras.2025.101581

[38] Biswal, G. and Meshram, G.S. (2025) Machine Learning-Based Prediction of Nusselt Number for Vertical Helical Coils in Natural Convection Heat Transfer. *International Communications in Heat and Mass Transfer*, **164**, Article ID: 108983. https://doi.org/10.1016/j.icheatmasstransfer.2025.108983

[39] Wang, R., Zeng, Z., Sadeq, A.M., Agrawal, M.K., Muhammad, T. and Rao, B.N. (2025) Predictive Performance Analysis of Machine Learning Models for Forced Convective Heat Transfer of a Flat-Plate in Counter-Rotating Cylinder Systems: A Comprehensive Evaluation. *Case Studies in Thermal Engineering*, **74**, Article ID: 106961. https://doi.org/10.1016/j.csite.2025.106961

[40] Tanzim, R., Das, A., Zaman, S.N., Lia, T.A. and Sarwar, S.T. (2025) A Chromosome Inspired Fin Structure for Microchannel Heat Sinks: CFD Driven XGBR, ANN, and MLR Models for Thermal and Fluid Flow Prediction. *International Communications in Heat and Mass Transfer*, **169**, Article ID: 109763. https://doi.org/10.1016/j.icheatmasstransfer.2025.109763